



# Parameterising continuum models of heat transfer in heterogeneous living skin using experimental data

*by*

**Sean McInerney**

Bachelor of Mathematics, 2017

School of Mathematical Sciences  
Faculty of Science and Engineering  
Queensland University of Technology

*Supervised by*

Matthew Simpson and Elliot Carr

A dissertation submitted in fulfilment  
of the requirements for the degree of  
Master of Philosophy

2018

**Keywords:** Burn injury; Heat transfer; Living skin; Experimental data; Parameter estimation; Experimental design.

In accordance with the requirements of the degree of Master of Philosophy in the School of Mathematical Sciences, I present the following thesis entitled,

**Parameterising continuum models of heat transfer in heterogeneous living  
skin using experimental data.**

This work was performed under the supervision of Matthew Simpson and Elliot Carr. I declare that this submission is my own work, except as acknowledged throughout the text, and has not been previously submitted for the award of any other degree or diploma at Queensland University of Technology or any other institution.

Signed,

Sean McInerney  
17 September 2018



## Acknowledgements

I would like to extend my deep gratitude for the guidance of my supervisors, Mat and Elliot. Their direction and support was instrumental in this research and my ability to complete this thesis.

I also thank Leila Cuttle, who introduced us to the problem that motivated much of our work.

It would be remiss of me to not acknowledge the Institute of Health and Biomedical Innovation, the School of Mathematical Sciences and ANZIAM, all of which provided me with the financial support necessary to travel to conferences. I appreciate the support greatly.

I will also take this opportunity to thank my family. The value that the love and support of my family consistently adds to my life can not be overstated. I hope that the family members who read this thesis find it interesting.



# Abstract

Burn injuries are relatively common and painful. To gain a better understanding of burns, mathematical models can be used to describe the associated heat transfer process. In this thesis, we present a simple continuum model that incorporates the layered, heterogeneous structure of skin tissue. The model comprises a skin layer and a fat layer with distinct, unknown thermal diffusivities. We then attempt to estimate the thermal diffusivities using experimental data. The experimental data is from a recent study into the heat conduction of living porcine (pig) tissue. One key feature of this data set is that all data is collected from a single location. This poses a problem for parameter inference; it is difficult to infer the behaviour in multiple layers of tissue when all data is extracted from just one of the layers. This thesis investigates experimental designs which optimise the precision with which we can calibrate the mathematical model, the different solution techniques to such a model and presents the algorithms and code used throughout the investigation. We find that a single probe is insufficient to accurately estimate the parameters in our layered continuum model, whereas two probes strategically placed makes precise parameter inference possible.



# Contents

<b>1</b>	<b>Introduction</b>	<b>1</b>
1.1	Overview . . . . .	1
1.2	Structure of this thesis . . . . .	6
1.3	Statement of joint authorship . . . . .	6
<b>2</b>	<b>Parameterising continuum models of heat transfer in heterogeneous living skin using experimental data</b>	<b>9</b>
2.1	Introduction . . . . .	13
2.2	Mathematical model . . . . .	16
2.3	Results and discussion . . . . .	19
2.3.1	Parameter inference: single probe . . . . .	20
2.3.2	Parameter inference: optimal placement of single probe . . . . .	25
2.3.3	Parameter inference: two probes . . . . .	29
2.3.4	Parameter inference: optimal placement of second probe . . . . .	31
2.4	Conclusions and future directions . . . . .	33
<b>3</b>	<b>Mathematical techniques for continuum models of heat transfer in heterogeneous living skin</b>	<b>37</b>
3.1	Mathematical model . . . . .	39
3.2	Model solution . . . . .	40
3.3	Numerical solution . . . . .	43
3.4	Solution verification . . . . .	46

<b>4 Conclusions</b>	<b>51</b>
4.1 Summary and Discussion . . . . .	51
4.2 Directions for Future Research . . . . .	52
<b>Bibliography</b>	<b>57</b>
<b>Appendix</b>	<b>63</b>

# Chapter 1

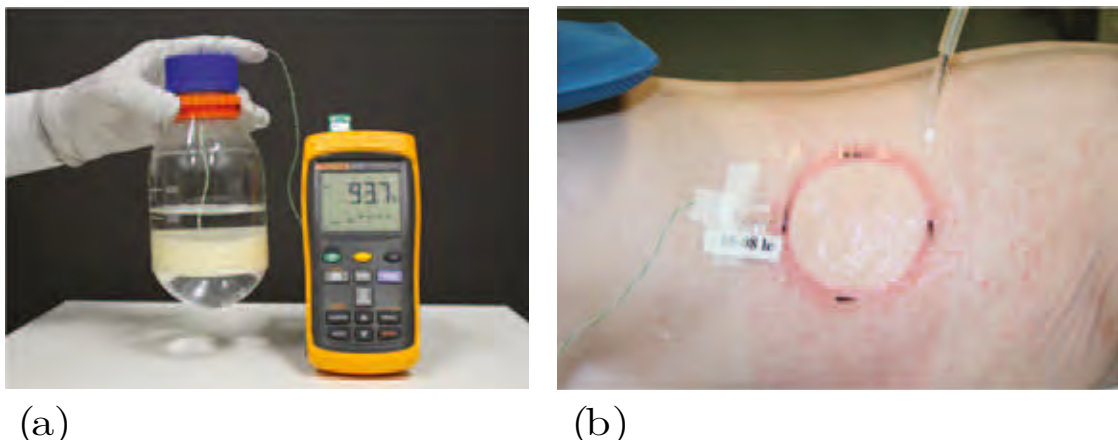
## Introduction

### 1.1 Overview

Burns are a common type of injury, particularly among young children (Li, 2017). Burn injuries are painful, result in scarring and may demand long-term treatment (Sheridan, 2012). The damage to the skin tissue inflicted by the burn can be mitigated by immediate treatment (Wood et al., 2016). Even after the initial burn, damage continues to occur as the heat propagates throughout the tissue. By quickly cooling down the tissue, the damage can be reduced. To gain a better understanding of this process and to gauge the efficacy of different treatment methods, experiments could be conducted on living animals. For ethical reasons, it is desirable to maximise the information garnered from these experiments. To this end, a sensible strategy is to develop a mathematical model that describes the heat transfer process, use the necessary number of experiments to determine the parameters of this model, then use the calibrated model to make predictions about a variety of scenarios.

Porcine skin tissue is accepted as being a reasonable approximation of human skin tissue, due to physiological similarities (Andrews et al., 2016; Abdullahi et al., 2014; Meyer et al., 1978; Montagna and Yun, 1964; Henriques and Moritz, 1947; Moritz and Henriques, 1947; Sullivan et al., 2001). In light of this, Cuttle and colleagues conducted heat transfer experiments on living pigs (Cuttle et al., 2006), as shown in Figure 1.1. Dr Cuttle is the Head of the Burns and Trauma Research Laboratory at the Centre for Children’s Health Research at Queensland University of Technology and was using the experiments to learn about tissue damage and the effect of different first aid treatments. In the experiments, a constant source of heat is applied to the surface of the skin tissue using a scalding device, with a single subdermal temperature probe recording data. After

the burn, treatment is applied to the surface of the inflicted area, often simply cool running water. The experiments vary design parameters such as duration of burn, temperature of the burn-inducing water, time of delay before treatment occurs and the temperature of the cool water acting as the first aid treatment. The investigation is extensive and many key findings from the experiments are published (Andrews et al., 2016; Cuttle et al., 2008a,b, 2010, 2006). However, the results are somewhat limited in the sense that the data is extracted at a single location in the tissue and any scenarios outside the exact design parameters of the conducted experiments are not considered. These limitations are understandably difficult to overcome from an experimentalist's point of view. Using more than one subdermal probe compromises the structural integrity of the thin skin tissue, which is approximately 4 mm thick, and only so many experiments of different designs can be conducted for ethical reasons. However, mathematical modelling tools can attempt to resolve both the issue of limited spatial sampling and the issue of limited experiments.




---

Figure 1.1: Porcine heat transfer experiments. (a) Scalding device. (b) Application of cool running water to the burn with subdermal temperature probe recording the temperature measurements. Images are reproduced from Simpson et al. (2017) with permission.

---

During the period of December 2016 to February 2017, I was involved in a summer research project, supervised jointly by Professor Simpson, Dr Carr and Dr Cuttle. The project aimed to develop a deeper insight into Dr Cuttle's experimental data by calibrating the solution of a simple heat transfer model to match the experimental observations. To describe the heat transfer in the living porcine tissue, we use a one-dimensional homogenised diffusion model. It is homogenised in the sense that we do not consider how the thermal diffusivity of the tissue varies spatially, using a single constant thermal diffusivity parameter. In this model, the temporal and spatial distribution of temperature,  $T(x, t)$ ,

is governed by,

$$\frac{\partial T(x, t)}{\partial t} = \alpha \frac{\partial^2 T(x, t)}{\partial x^2} + \beta(T(x, t) - T_0), \quad (1.1)$$

for  $0 < x < H$  and  $t > 0$ , subject to the following initial and boundary conditions:

$$T(x, 0) = T_0, \quad (1.2)$$

$$T(0, t) = \begin{cases} T_h, & 0 < t < 15, \\ T_c, & 15 < t < 15 + t_d, \end{cases} \quad (1.3)$$

$$\frac{\partial T(H, t)}{\partial x} = \gamma(T_0 - T(H, t)), \quad (1.4)$$

where  $H$  is the total depth of the tissue including the epidermis, dermis and fat,  $t_d$  is the duration for which the treatment is applied,  $\alpha$  is the thermal diffusivity,  $\beta$  is a heat transfer coefficient governing the rate at which thermal energy is lost to the blood supply,  $T_0$  is a reference temperature which we take to be approximately equal to the temperature of the blood and muscle,  $T_h$  is the temperature of the heat source used to create the burn,  $T_c$  is the temperature of the first aid treatment, and  $\gamma$  is a heat transfer coefficient governing the rate at which thermal energy is lost to the adjacent muscle at  $x = H$ . The unknown parameters of this model,  $\alpha$ ,  $\beta$  and  $\gamma$ , were calibrated to the experimental data, allowing us to predict the thermal behaviour of the skin tissue at all locations and for different experimental designs. The model calibration and prediction is presented in Figure 1.2, Figure 1.2(a) presents the homogenised model as a simple schematic, Figure 1.2(b)-(c) shows the calibrated mathematical model plotted against the experimental data at the probe location ( $x = 4\text{ mm}$ ) and Figure 1.2(d)-(e) presents the solution of the mathematical model for  $0 \leq x \leq 4$  at various points in time throughout the heating and cooling process. This mathematical model could then be utilised to investigate scenarios outside the specificities of the experiments conducted, such as different temperatures of the scalding water, different temperatures of the cooling water and different burn durations. In Simpson et al. (2017), we use the mathematical model to study the effect of temperature of the cooling water on the potential damage inflicted on the skin tissue.

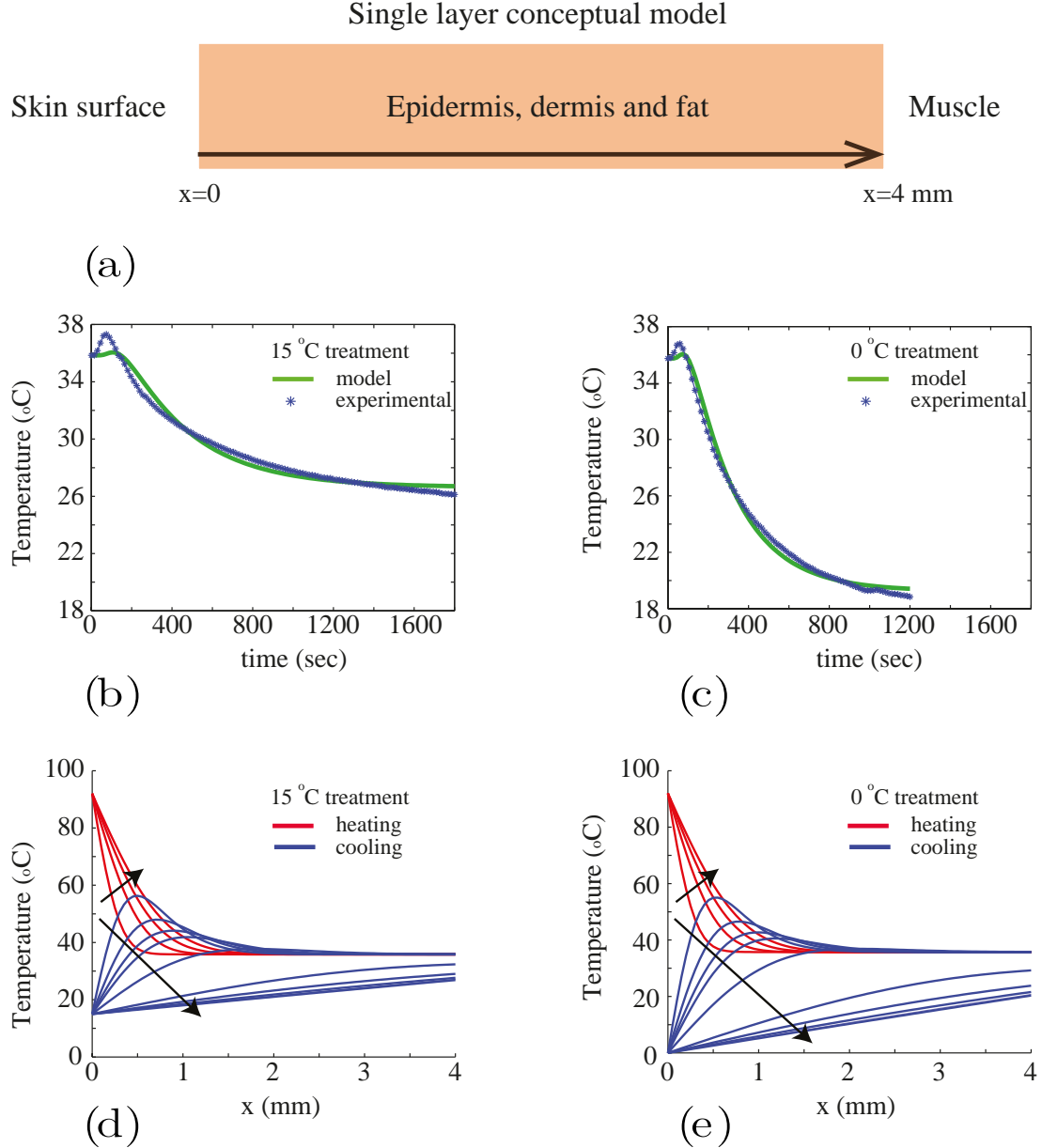
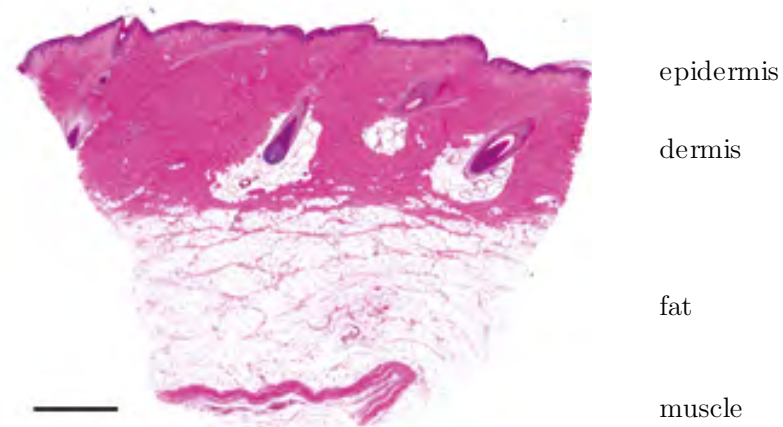


Figure 1.2: Calibration of the single layer model and solution visualisation. (a) Schematic of the homogenised model. The depth of the tissue is denoted  $x$ . (b-c) Calibration of mathematical model to experimental data for two different treatment conditions. (d-e) Solution of calibrated mathematical model showing spatial and temporal variations in the temperature distribution during both the heating (red) and cooling (blue) phases of experiments for two different treatment conditions. The direction of the arrow indicates the forward progression of time. Images are reproduced from Simpson et al. (2017) with permission.

As with any investigation utilising a mathematical model, the results hinge on the validity of the assumptions made when developing the model. One concern with the mathematical model used was that it treated the tissue as a single homogeneous layer. This was viewed as necessary due to the fact that the experimental data used to calibrate the model is extracted from a single location in the tissue. It was hypothesised that trying to deduce the thermal behaviour in multiple layers would be difficult, if not impossible, using only information retrieved from one of the layers.




---

Figure 1.3: Histological image of normal porcine skin. Scale bar is 1 mm. Image is reproduced from Simpson et al. (2017) with permission.

---

It is well known, however, that skin is layered (Johnson et al., 1997; van der Merwe et al., 2006), as illustrated in Figure 1.3. This motivates us to develop a more sophisticated mathematical model for heat transfer in living tissue that incorporates the layered structure of skin. For this model to be useful in predicting real life behaviour, we must have accurate estimates of the parameters in the model. However, it may be difficult to calibrate a heterogeneous model using data obtained from a single location.

The aims of this thesis are to:

1. develop and solve a mathematical model that describes the heat transfer process of living skin that incorporates the layered structure inherent with skin tissue;
2. determine whether it is possible to parameterise the model using experimental data extracted from a single location in the tissue; and

3. investigate how modifying the experimental design could improve the precision with which the model parameters are inferred.

## 1.2 Structure of this thesis

The substance of this thesis corresponds to a scientific manuscript accepted for publication by the editor-in-chief (as of September 14, 2018) at the *International Journal of Heat and Mass Transfer*. Chapter 2 of this thesis is the main document of the paper. Chapter 3 is a portion of the supplementary material which outlines the mathematical techniques.

In Chapter 2, we explore the process of parameterising a continuum model of heat transfer in heterogeneous living skin with spatially limited experimental data. To describe the heat transfer, we present a simplified two-layer mathematical model, comprising a skin and fat layer with unknown thermal diffusivities. In past research, *in vivo* porcine heat conduction experiments have been conducted, with a single subdermal temperature probe extracting data from the bottom of the fat tissue. Synthetic data is developed to mimic the *in vivo* porcine experimental data. We demonstrate that precise inference of the two parameters in our mathematical model - the thermal diffusivities of skin and fat - is impossible using a single probe located at the bottom of the fat tissue. We then explore how the use of a second probe could improve the parameter inference process and suggest the optimal location for this second probe.

In Chapter 3, we detail the solution methodology for the two-layer mathematical model utilised in Chapter 2. This approach involves taking the Laplace transform of the governing equations and boundary conditions in the model, finding the solution of the Laplace transform system of equations in each layer and then performing the inverse Laplace transform numerically to obtain the solution of the original two-layer mathematical model. To verify the accuracy of the solution, a finite volume scheme is also presented in detail. We find that the Laplace approach and the finite volume scheme produces visually indistinguishable solutions across a variety of different parameters.

In Chapter 4, we review the key findings of this thesis and discuss possible future avenues of research.

## 1.3 Statement of joint authorship

This section outlines the contribution of the Masters student in relation to the co-authors of the joint work presented in this thesis.

**Chapter 2: Parameterising continuum models of heat transfer in heterogeneous living skin**

This chapter corresponds to the main document of the paper titled “Parameterising continuum models of heat transfer in heterogeneous living skin using experimental data”, accepted for publication by the editor-in-chief (as of September 14, 2018) at the *International Journal of Heat and Mass Transfer*. The co-authors of this paper are Sean McInerney, Elliot Carr and Matthew Simpson. Their contributions to this chapter are listed below.

- Sean McInerney performed the analysis, generated the figures and drafted the manuscript.
- Elliot Carr jointly coordinated the research project, supervised the analysis and generation of figures, and provided feedback on the drafting of the manuscript.
- Matthew Simpson jointly coordinated the research project, supervised the analysis and generation of figures, and helped draft the manuscript.

**Chapter 3: Mathematical Techniques for continuum models of heat transfer in heterogeneous living skin**

This chapter corresponds to the mathematical techniques portion of the supplementary material of the paper titled “Parameterising continuum models of heat transfer in heterogeneous living skin using experimental data”, accepted for publication by the editor-in-chief (as of September 14, 2018) at the *International Journal of Heat and Mass Transfer*. The contributions of the authors are listed below.

- Sean McInerney implemented the mathematical techniques, generated the figures and drafted the manuscript.
- Elliot Carr developed the solution to the model, supervised the implementation of the mathematical techniques and the generation of figures, and provided feedback on the drafting of the manuscript.
- Matthew Simpson supervised the implementation of the mathematical techniques and the generation of figures, and helped draft the manuscript.



## Chapter 2

# Parameterising continuum models of heat transfer in heterogeneous living skin using experimental data

This chapter comprises the main text of the following manuscript:

S McInerney, EJ Carr and MJ Simpson, Parameterising continuum models of heat transfer in heterogeneous living skin using experimental data, *International Journal of Heat and Mass Transfer*, accepted for publication, September 2018.



## Abstract

In this work we consider a recent experimental data set describing heat conduction in living porcine tissues. Understanding this novel data set is important because porcine skin is similar to human skin. Improving our understanding of heat conduction in living skin is relevant to understanding burn injuries, which are common, painful and can require prolonged and expensive treatment. A key feature of skin is that it is layered, with different thermal properties in different layers. Since the experimental data set involves heat conduction in thin living tissues of anaesthetised animals, an important experimental constraint is that the temperature within the living tissue is measured at one spatial location within the layered structure. Our aim is to determine whether this data is sufficient to reliably infer the heat conduction parameters in layered skin, and we use a simplified two-layer mathematical model of heat conduction to mimic the generation of experimental data. Using synthetic data generated at one location in the two-layer mathematical model, we explore whether it is possible to infer values of the thermal diffusivity in both layers. After this initial exploration, we then examine how our ability to infer the thermal diffusivities changes when we vary the location at which the experimental data is recorded, as well as considering the situation where we are able to monitor the temperature at two locations within the layered structure. Overall, we find that our ability to parameterise a model of heterogeneous heat conduction with limited experimental data is very sensitive to the location where data is collected. Our modelling results provide guidance about optimal experimental design that could be used to guide future experimental studies.



## 2.1 Introduction

Injuries caused by accidental exposure to hot liquids are common, painful and often require extensive long-term treatment (Sheridan, 2012). To improve our understanding of how thermal energy propagates through human skin, experimental studies often work with porcine (pig) skin because porcine skin is anatomically similar to human skin (Andrews et al., 2016; Abdullahi et al., 2014; Meyer et al., 1978; Montagna and Yun, 1964; Henriques and Moritz, 1947; Moritz and Henriques, 1947; Sullivan et al., 2001). Many experimental studies deal with heat conduction in excised non-living tissues (Henriques and Moritz, 1947; Moritz and Henriques, 1947; El-Brawany et al., 2009; Brown et al., 1993). In contrast, the experimental protocols developed by Cuttle and colleagues (Cuttle et al., 2006, 2008a,b, 2010) are unique because they quantify heat conduction in living porcine tissues. Working with living tissues is far more biologically relevant than working with excised non-living tissues. Cuttle's experimental protocol involves working with anaesthetised living pigs that are given analgesia. A thermocouple probe, referred to as the *subdermal probe*, is inserted obliquely under the skin of the animal at various locations on the body (Cuttle et al., 2006, 2008a,b, 2010). To initiate an experiment, a cylindrical scald creation device is placed onto the surface of the skin so that the centre of the circular scald device is above the subdermal probe. Pre-heated water is pumped into the scald device and suctioned out of the device at an equal rate to ensure that a constant level of water at a particular temperature is maintained in the device at all times during the experiment. The temperature response in the living skin is measured by the subdermal probe as a function of time during the experiment. This time series data reveals information about how the thermal energy propagates through the living skin, and this experimental protocol can be used to study how thermal energy propagates through skin in different locations on the body. Further, by using pigs of different ages the same experimental protocol can be used to study how the propagation of thermal energy depends on skin thickness (Andrews et al., 2016).

A visual summary of Cuttle's experimental porcine model is given in Figure 2.1. The image in Figure 2.1(a) shows a portion of excised skin at the conclusion of an experiment highlighting the location and size of the subdermal probe. The histology image in Figure 2.1(b) highlights the layered structure of the skin. The epidermis and dermis forms the upper layer of the skin where hair follicles are present (Haridas et al., 2017, 2018). The epidermis and dermis are bright pink in Figure 2.1(b), and throughout this study we treat the epidermis and dermis as a single layer that we call the *skin* layer. Underneath the skin

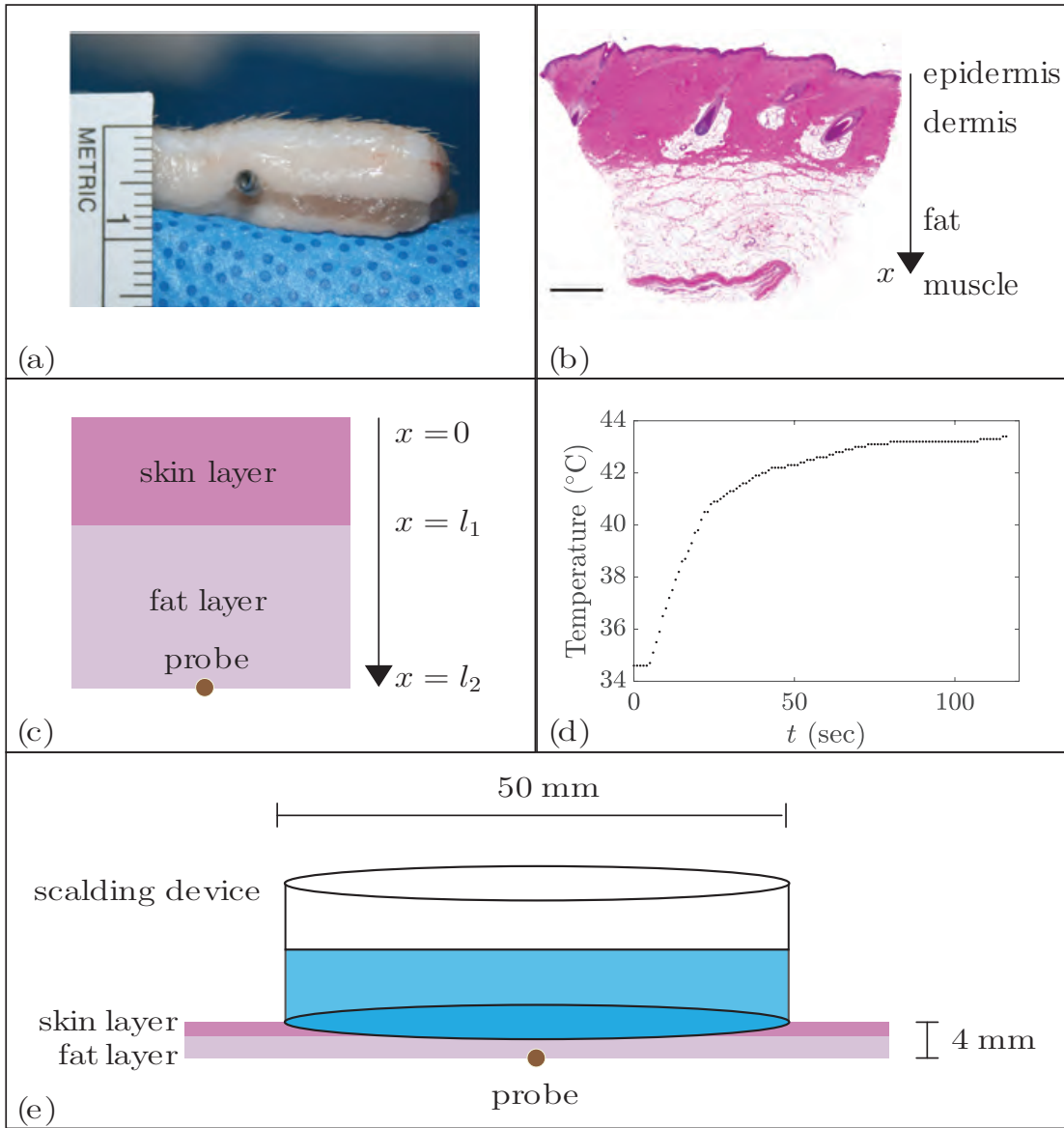


Figure 2.1: Developing a two-layer heterogeneous mathematical model to mimic the experimental porcine model. (a) Excised skin, showing the location of the probe and the depth of the tissue. (b) Histological image of normal porcine skin. Scale bar is 1 mm. The depth below the surface of the skin is denoted by  $x \geq 0$ . (c) Conceptual two-layer model of the tissue with a skin layer (bright pink) sitting above the fat layer (lighter pink). The interface between the two layers is at  $x = l_1$ , and the probe is located at the bottom of the fat layer,  $x = l_2$ . (d) Example of the temporal variation of dimensional temperature,  $\hat{T}(l_2, t)$ , reported in Simpson et al. (2017). Data is obtained from a subdermal temperature probe at  $x = l_2$ . The water in the scald creation device is held at 50° C for a duration of 120 s. (e) Schematic showing that the tissues are very thin (4 mm) compared to the diameter of the scald creation device (50 mm). Images in (a) and (b) are reproduced from Simpson et al. (2017) with permission.

layer there is a layer of fat that is a lighter shade of pink in Figure 2.1(b). Throughout this work we refer to this lower layer as the *fat* layer. As indicated in Figure 2.1(c), we adopt a coordinate system where  $x = 0$  corresponds to the skin surface. The interface between the fat and skin is located at  $x = l_1 > 0$ , we have  $l_1 = 1.6$  mm in this case. The interface between the fat and the underlying muscle and bone is at  $x = l_2 > l_1$ , and we have  $l_2 = 4.0$  mm in this case. Our conceptual idealisation of the structure of the layered tissues is given in Figure 2.1(c) where the subdermal probe is placed at  $x = l_2$  since experimental data reported by Cuttle involves placing the probe at the bottom of the fat layer (Andrews et al., 2016; Simpson et al., 2017). A summary of the kind of experimental data reported by Cuttle is given in Figure 2.1(d). In this particular experiment the probe is located at the interface of the fat and muscle,  $x = l_2$ , and a scald creation device of diameter 50 mm is placed on the surface of the skin (Andrews et al., 2016). Water at temperature of 50° C is maintained in the scald creation device for a duration of 120 s, and the time series data showing the temperature at the subdermal probe is recorded, as shown. It is worth noting that the total depth of the tissue (4 mm) is much smaller than the diameter of the scald creation device (50 mm), so that  $4/50 = 0.08 \ll 1$ , as illustrated in Figure 2.1(e). Since the centre of the circular scald creation device is placed directly over the location of the probe the heat transfer downward through the skin can be idealised as a one-dimensional process (Simpson et al., 2017).

A prominent feature of the skin, highlighted in Figure 2.1(b), is the layered structure where we see that the fat layer is below the skin layer. This kind of histological information has been previously incorporated into mathematical descriptions of heat transfer in skin by explicitly accounting for the layered, heterogeneous structure of the tissue. These previous models have often been based on generalisations of Pennes' bioheat equation (Pennes, 1948; Kengne and Lakhssassi, 2015; Mercer and Sidhu, 2006) and re-formulated as a multilayer heterogeneous heat transfer model where the thermal properties can vary between the different layers (Diller et al., 1991; Baldwin et al., 2012; Orgill et al., 1998; Orndorff et al., 2017; Sarker et al., 2015). A key limitation of working with such a heterogeneous multilayer heat transfer model is that they are more challenging to parameterise than simpler single layer models. This is a consequence of the fact that there are a greater number of unknown parameter values in a multilayer heterogeneous model compared to a simpler single layer model of heat transfer. This challenge is particularly acute if we consider parameterising a mathematical model of heat transfer using Cuttle's realistic experiments that report the temperature response at one location within the layered structure. This experimental limitation is difficult to overcome because inserting multiple probes simultaneously at different depths would risk compromising the integrity of the living tissues. Our previous work has involved calibrating the solution of much simpler single layer homo-

geneous models to match data from Cuttle's experiments (Andrews et al., 2016; Simpson et al., 2017). However, these previous studies suffer from the limitation that they implicitly treat the thermal parameters of the skin layer and fat layer together into a simplified, vertically averaged, homogenised single layer (Simpson, 2009). While this approach is mathematically convenient, it is unclear whether a single layer model is appropriate since we know that one of the main biological roles of the fat layer is to provide thermal insulation (Hayward and Keatinge, 1981). Therefore, we expect that the thermal properties of the skin and fat layers could be very different.

In this work we use a two-layer heterogeneous model to describe heat conduction in living tissues. Our aim is to perform a suite of synthetic experiments with realistic parameter values to mimic data generated by Cuttle's experimental protocol. With this synthetic data we explore the extent to which we can confidently estimate the thermal diffusivity in each layer when we have limited experimental observations where the temperature is reported at one single location within the layered tissues. To achieve this, we use the solution of the two-layer heterogeneous model, parameterised with biologically-relevant estimates of the thermal diffusivity of skin and fat, to generate synthetic data that mimics Cuttle's experimental protocol where a single probe is placed at the bottom of the fat layer. Given that the synthetic data is generated with known estimates of the thermal diffusivity in the skin and fat layers, we then systematically explore the parameter space to investigate whether the kind of data can be used to reliably determine parameters in the heterogeneous mathematical model. Once we have demonstrated how delicate this parameter estimation task can be, we turn our attention to the question of experimental design. First, we explore whether our ability to determine the parameters in the two-layer model varies when we alter the location of the single subdermal probe. Second, we explore the extent to which our ability to estimate the parameters improves when we consider synthetic experiments with two probes so that the temperature is recorded simultaneously at two different positions within the layered skin.

## 2.2 Mathematical model

We model the transfer of heat through the skin and fat layers using a one-dimensional model. This is a reasonable assumption given that the depth of the tissue is much smaller than the width of the scald creation device used in Cuttle's experimental protocol (Andrews et al., 2016; Simpson et al., 2017). If the tissue depth was comparable to the diameter of the scald creation device it would be more appropriate to use a two- or three-dimensional mathematical model. In this work we assume that the temporal and spatial distributions of dimensional temperature in the skin layer,  $\mathcal{T}_1(x, t)$ , and the fat

layer  $\mathcal{T}_2(x, t)$ , are governed by

$$\frac{\partial \mathcal{T}_1(x, t)}{\partial t} = D_1 \frac{\partial^2 \mathcal{T}_1(x, t)}{\partial x^2}, \quad 0 < x < l_1, \quad (2.1)$$

$$\frac{\partial \mathcal{T}_2(x, t)}{\partial t} = D_2 \frac{\partial^2 \mathcal{T}_2(x, t)}{\partial x^2}, \quad l_1 < x < l_2, \quad (2.2)$$

where  $D_1 > 0$  is the thermal diffusivity of the skin and  $D_2 > 0$  is the thermal diffusivity of fat. We have not included any source terms in Equations (2.1)-(2.2). Although some previous studies have incorporated source terms to account for the transfer of thermal energy from the skin tissues to the blood supply (Pennes, 1948), known as perfusion, our previous work, in which we calibrated the solution of a single layer model to match data from Cuttle's experiments suggests that the role of perfusion is negligible in these experiments (Simpson et al., 2017). We note that the assumption that perfusion plays a negligible role has also been adopted in other modelling studies (Diller et al., 1991).

Experimental data suggests that the initial variation in temperature with depth is negligible (Andrews et al., 2016). Therefore we choose the initial condition to be

$$\mathcal{T}_1(x, 0) = \mathcal{T}_0, \quad 0 < x < l_1, \quad (2.3)$$

$$\mathcal{T}_2(x, 0) = \mathcal{T}_0, \quad l_1 < x < l_2, \quad (2.4)$$

where  $\mathcal{T}_0$  is the initial dimensional temperature of the skin and fat layers.

The boundary condition at  $x = 0$  corresponds to the placement of the scald creation device on the skin surface. Cuttle's experimental protocol carefully maintains a constant temperature in the scald creation device by pumping water of a constant temperature into the device at the same rate as water is pumped from the device, thus ensuring the maintenance of a constant temperature at the skin surface (Andrews et al., 2016). Therefore, we represent this as a Dirichlet boundary condition at  $x = 0$ . For simplicity, we assume that the flux of thermal energy at the base of the fat layer,  $x = l_2$ , is negligible and we will comment on the validity of this assumption in Section 2.4. Together, these boundary conditions are incorporated into the model by specifying

$$\mathcal{T}_1(0, t) = \mathcal{T}_h, \quad (2.5)$$

$$\frac{\partial \mathcal{T}_2(l_2, t)}{\partial x} = 0. \quad (2.6)$$

where  $\mathcal{T}_h$  is the dimensional temperature of the water in the scald creation device.

In the literature, there are several different interface conditions that can be implemented in multilayer models of heat transfer (Carr and Turner, 2016; Carr et al., 2017;

Rodrigo and Worthy, 2016; Sheils and Deconinck, 2014; Sheils, 2017). Here we take the simplest, most fundamental approach by assuming perfect contact between the skin and fat layers. This amounts to assuming that the temperature and the flux of thermal energy are continuous at the interface

$$\mathcal{T}_1(l_1, t) = \mathcal{T}_2(l_1, t), \quad (2.7)$$

$$D_1 \frac{\partial \mathcal{T}_1(l_1, t)}{\partial x} = D_2 \frac{\partial \mathcal{T}_2(l_1, t)}{\partial x}. \quad (2.8)$$

An attractive feature of Cuttle's experimental design is that the temperature of the water in the scald creation device can be easily altered (Andrews et al., 2016; Simpson et al., 2017). For example, this experimental protocol has been used previously to study how skin responds to different temperature burns by using water at 50° C, 55° C and 60° C in the scald creation device (Andrews et al., 2016). Therefore, to ensure that our analysis can easily incorporate this feature of the experiments we non-dimensionalise the dependent variable in Equations (2.1)-(2.8) so that all of these different experimental conditions can be represented by the same mathematical model without explicitly considering the role of  $\mathcal{T}_h$ . To non-dimensionalise the dependent variable we introduce

$$T_1(x, t) = \frac{\mathcal{T}_1(x, t) - \mathcal{T}_0}{\mathcal{T}_h - \mathcal{T}_0}, \quad (2.9)$$

$$T_2(x, t) = \frac{\mathcal{T}_2(x, t) - \mathcal{T}_0}{\mathcal{T}_h - \mathcal{T}_0}, \quad (2.10)$$

where  $T_1(x, t) \in [0, 1]$  is the non-dimensional temperature in the skin layer and  $T_2(x, t) \in [0, 1]$  is the non-dimensional temperature in the fat layer. Re-writing the governing equations in terms of these non-dimensional variables gives

$$\frac{\partial T_1(x, t)}{\partial t} = D_1 \frac{\partial^2 T_1(x, t)}{\partial x^2}, \quad 0 < x < l_1, \quad (2.11)$$

$$\frac{\partial T_2(x, t)}{\partial t} = D_2 \frac{\partial^2 T_2(x, t)}{\partial x^2}, \quad l_1 < x < l_2. \quad (2.12)$$

The initial condition for the non-dimensional model is

$$T_1(x, 0) = 0, \quad (2.13)$$

$$T_2(x, 0) = 0, \quad (2.14)$$

and the relevant boundary conditions are

$$T_1(0, t) = 1, \quad (2.15)$$

$$\frac{\partial T_2(l_2, t)}{\partial x} = 0. \quad (2.16)$$

Finally, the interface conditions are written as

$$T_1(l_1, t) = T_2(l_1, t), \quad (2.17)$$

$$D_1 \frac{\partial T_1(l_1, t)}{\partial x} = D_2 \frac{\partial T_2(l_1, t)}{\partial x}. \quad (2.18)$$

Equations (2.11)-(2.18) constitute the mathematical model that we consider in this study. For any particular choice of  $D_1$  and  $D_2$ , the model can be solved to predict the temporal and spatial distribution of non-dimensional temperature within the two-layer problem,  $T_1(x, t)$  and  $T_2(x, t)$ . These non-dimensional temperature profiles can be re-scaled, according to Equations (2.9)-(2.10), to give  $\mathcal{T}_1(x, t)$  and  $\mathcal{T}_2(x, t)$ , which represent any particular experimental condition characterised by different choices of  $\mathcal{T}_0$  and  $\mathcal{T}_h$ . A convenient feature of the mathematical model is that Equations (2.11)-(2.18) can be solved, very efficiently, using Laplace transforms (Debnath and Bhatta, 2007). This Laplace transform solution can be evaluated at little computational cost, regardless of the choice of  $D_1$ ,  $D_2$ ,  $l_1$  and  $l_2$ . A full description of the Laplace transform solution technique, and validation of the accuracy of this approach is given in Chapter 3. Algorithms and code used in this work are available in the Appendix.

## 2.3 Results and discussion

Throughout this work we consider a fixed tissue geometry by setting  $l_1 = 1.6$  mm and  $l_2 = 4.0$  mm, which match the histology measurements in Figure 2.1(a)-(b). To solve Equations (2.11)-(2.18) we must specify  $D_1$  and  $D_2$ . Our approach is to:

1. Select biologically-relevant estimates of the target parameters,  $(\hat{D}_1, \hat{D}_2)$ ;
2. Solve Equations (2.11)-(2.18) with the target parameters;
3. Extract time series data from the solution generated in Step 2 so that the synthetic data from the mathematical model is consistent with Cuttle's experimental data;
4. Explore the solutions of Equations (2.11)-(2.18) across the  $(D_1, D_2)$  parameter space to assess how well we could estimate  $(\hat{D}_1, \hat{D}_2)$  using the synthetic data generated in Step 3; and

5. Use the mathematical modelling tools to explore whether we can optimise the experimental design to improve our ability to reliably estimate  $(\hat{D}_1, \hat{D}_2)$ .

### 2.3.1 Parameter inference: single probe

To generate synthetic data we must first estimate target parameters,  $(\hat{D}_1, \hat{D}_2)$ . Previous work that interprets data from Cuttle's experiments with a simplified, single-layer, homogenised mathematical model leads to an estimate of the homogenised effective thermal diffusivity,  $D_{\text{eff}} = 0.014 \text{ mm}^2/\text{s}$ . We will use this estimate to guide our choice of  $(\hat{D}_1, \hat{D}_2)$ . To achieve this we assume that  $D_{\text{eff}}$  corresponds to the homogenised thermal diffusivity of the two-layer tissue that is given by a weighted harmonic mean,  $l_2/D_{\text{eff}} = (l_2 - l_1)/\hat{D}_1 + l_2/\hat{D}_2$  (Carr et al., 2017). In addition, we make use of the fact that a key physiological role of the fat layer is to provide thermal insulation (Hayward and Keatinge, 1981). Therefore, we incorporate this into our heterogeneous multilayer model by requiring that  $D_2 < D_1$ , and we set  $\hat{D}_1 = 10 \hat{D}_2$  to reflect this. Combining these two biologically-motivated assumptions gives  $\hat{D}_1 = 0.09 \text{ mm}^2/\text{s}$  and  $\hat{D}_2 = 0.009 \text{ mm}^2/\text{s}$ , and we hold these target parameters constant throughout this work.

The solution of Equations (2.11)-(2.18) parameterised with  $(D_1 = \hat{D}_1, D_2 = \hat{D}_2)$  is shown in Figure 2.2(a). Here, the initial temperature is zero, and we see that energy is introduced into the system through the Dirichlet boundary at  $x = 0 \text{ mm}$ , for  $t > 0$ . As the solution evolves, the temperature is continuous at the interface but the spatial gradient of temperature is discontinuous at the interface. From a modelling perspective, it is natural for us to visualise the entire spatial and temporal features of the solution of Equations (2.11)-(2.18) in Figure 2.2(a). However, this level of detail is not available in Cuttle's experimental protocol (Cuttle et al., 2006, 2008a,b, 2010) because temperature is measured at one spatial location only. Therefore, to ensure that the synthetic data we extract from the solution of Equations (2.11)-(2.18) is compatible with Cuttle's experimental data, we use the solution of the mathematical model to generate time series data, showing  $T_2(l_2, t)$ , at one spatial location only. At first we focus on  $x = l_2$  as the probe is placed at the bottom of the fat layer in the experiments (Andrews et al., 2016; Simpson et al., 2017). Later, in Section 2.3.2, we also consider the influence of varying the location of the probe.

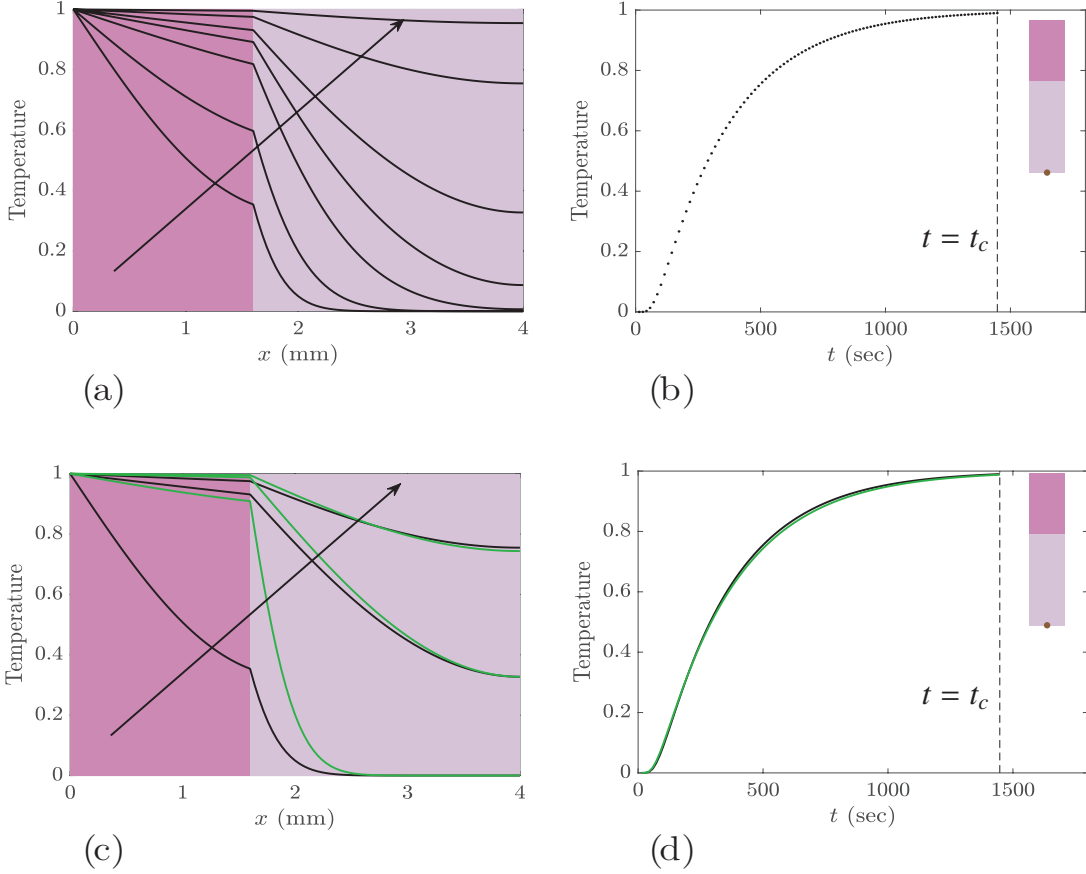


Figure 2.2: Solutions to Equations (2.11)-(2.18) for  $l_1 = 1.6$  mm and  $l_2 = 4$  mm. In (a) we set the thermal diffusivities to be the target parameters,  $\hat{D}_1 = 0.09$  mm<sup>2</sup>/s and  $\hat{D}_2 = 0.009$  mm<sup>2</sup>/s. The solutions of Equations (2.11)-(2.18) are plotted at  $t = 10, 20, 50, 100, 200, 500$  and 1000 s, with the arrow showing the direction of increasing  $t$ . (b) Synthetic time series data,  $\hat{T}(l_2, t)$ , shows the temperature at the location of the probe,  $x = l_2$ . The time series is constructed using 100 equally-spaced time point between  $t = t_c/100$  and  $t = t_c$ , where  $t_c = 1447.5$  s. (c) Comparison of  $T_1(x, t)$  and  $T_2(x, t)$  for two different parameter pairs. The black curves show the solution using the target parameters,  $\hat{D}_1 = 0.09$  mm<sup>2</sup>/s and  $\hat{D}_2 = 0.009$  mm<sup>2</sup>/s, and the green curves show solutions of the same model for a very different choice of parameters,  $D_1 = 0.45$  mm<sup>2</sup>/s and  $D_2 = 0.0077$  mm<sup>2</sup>/s. In (c) solutions are shown at  $t = 10, 200$  and 500 s with the arrow showing the direction of increasing  $t$ . (d) Comparison of time series  $\hat{T}(l_2, t)$  (black) and  $T(l_2, t)$  (green), over the interval  $0 \leq t \leq t_c$ , using the spatiotemporal solutions in (c). The bright pink and lighter pink background colours in (a) and (c) are chosen to correspond with the colour of the skin and fat layers in Figure 2.1(b). Subfigures (b) and (d) contain an inset showing the geometry of the skin layers with the brown circle showing the location of the probe,  $x = l_2$ . In (b) and (d), the vertical dashed black line indicates the critical time,  $t_c$ .

To construct the time series data from the solution of Equations (2.11)-(2.18), we must first decide on the interval of time that we will focus on. Since our aim is to estimate  $D_1$  and  $D_2$ , it is useful to recall that an estimate of the duration of time required for the solution of Equations (2.11)-(2.18) to asymptote to the corresponding steady state solution will depend upon  $D_1$  and  $D_2$  (Carr and Simpson, 2018; Simpson, 2017; Landman and McGuinness, 2000). This duration of time, called the *critical time* (Hickson et al., 2009a,b), can be estimated by calculating the time required for the transient solution to reach within some small tolerance of the corresponding steady solution. For our choice of boundary conditions the long-time steady state solution of Equations (2.11)-(2.18) is  $\lim_{t \rightarrow \infty} T_1(x, t) = \lim_{t \rightarrow \infty} T_2(x, t) = 1$ . In this work we denote the critical time as  $t_c$ , and we estimate the critical time by calculating  $t_c$  that satisfies  $T_2(l_2, t_c) = 0.99$ , corresponding to a tolerance of 1%. For our values of  $l_1$ ,  $l_2$ ,  $\hat{D}_1$  and  $\hat{D}_2$  we have  $t_c = 1447.5$  s. In this work we treat  $l_1$ ,  $l_2$ ,  $\hat{D}_1$  and  $\hat{D}_2$  as constants which means that  $t_c$  is also a constant throughout this study. With our estimate of the critical time we generate the time series  $T_2(l_2, t_j)$  with  $t_j = j\delta t$ , where  $j = 1, 2, \dots, 100$  and  $\delta t = t_c/100$  s. This time series simply corresponds to 100 equally-spaced time points between  $t = t_c/100$  and  $t = t_c$ , and we visualise this time series in Figure 2.2(b) for the problem shown previously in Figure 2.2(a). This time series confirms that  $T_2(l_2, 0) = 0$ , and  $T_2(l_2, t)$  approaches unity as  $t$  increases.

Now that we have specified the target parameters,  $(\hat{D}_1, \hat{D}_2)$ , and defined how we extract synthetic data from the solution Equations (2.11)-(2.18), we explore how well we can estimate  $(D_1, D_2)$  so that the time series of  $T_2(l_2, t)$  matches the synthetic data. Ideally, there would be a unique choice of  $(D_1, D_2)$  for which the solution of the model matches the synthetic time series data. However, in practice we find there is large range of parameter pairs,  $(D_1, D_2)$ , for which the time series data matches the synthetic time series data remarkably well. To illustrate this we show solutions of Equations (2.11)-(2.18) with very different choice of  $(D_1, D_2)$  in Figure 2.2(c). Here, we show the full spatial profile of the two solutions and it is obvious, from visual inspection alone, that the two solutions are very different. However, for these same two solutions, we see almost no difference when we view the time series,  $T_2(l_2, t)$ , in Figure 2.2(d). This observation suggests that data provided by Cuttle's experimental protocol might not be appropriate to constrain estimates of  $(D_1, D_2)$ . This would be particularly challenging since Cuttle's data will also be subject to experimental, biological and measurement variability that we have not accounted for in Figure 2.2. For simplicity and clarity, throughout this study we neglect the influence of such experimental variability, and we will comment on this assumption later, in Section 2.4.

Since the two time series in Figure 2.2(d) are difficult to visually distinguish, we introduce a discrepancy measure to assist in distinguishing between these time series quan-

titatively. In this work we use

$$d(D_1, D_2|p) = \sum_{j=1}^{100} \left| \widehat{T}(p, t_j) - T(p, t_j) \right|, \quad (2.19)$$

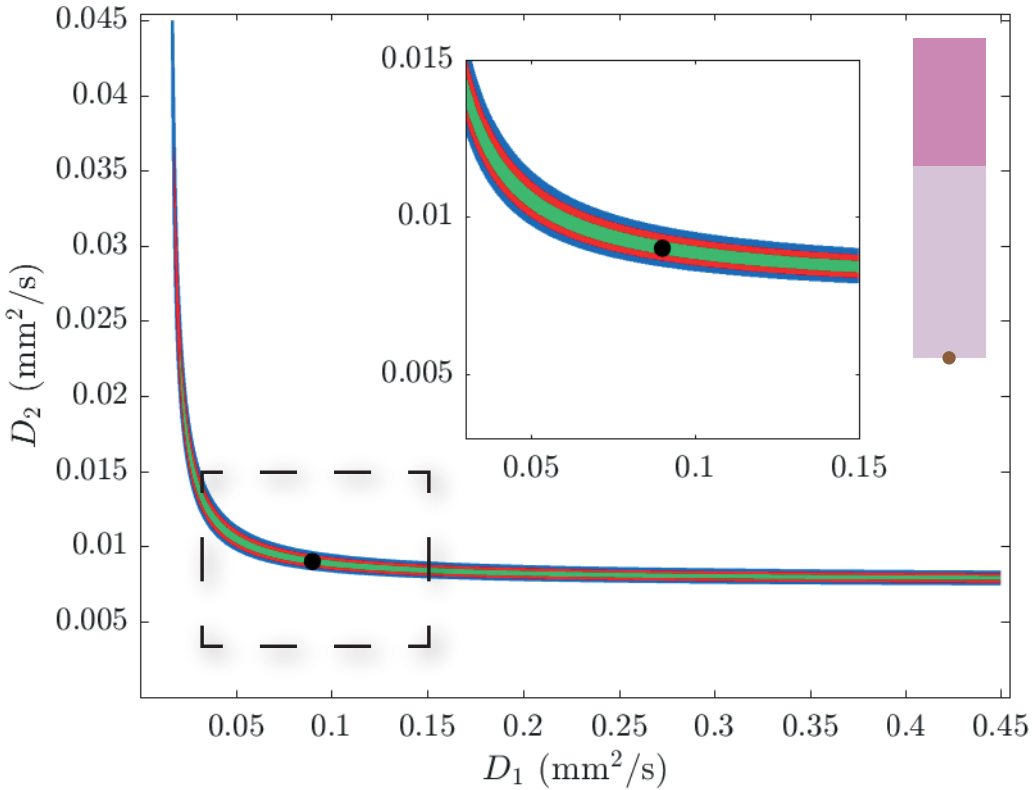
where  $\widehat{T}(p, t_j)$  is the solution of Equations (2.11)-(2.18) parameterised with the target parameters  $(\widehat{D}_1, \widehat{D}_2)$ , at location  $x = p$  and at time  $t = t_j$ , and  $T(p, t_j)$  is the solution of Equations (2.11)-(2.18), with some other choice of  $(D_1, D_2)$ , at location  $x = p$  and at time  $t = t_j$ . Here the sum is taken over 100 equally-spaced time points from  $t = t_c/100$  to  $t = t_c$  where  $t_c$  is first calculated for each choice of  $(D_1, D_2)$  that we consider. The key feature of this discrepancy measure is that there is a single probe at location  $x = p$ . Intuitively, we expect that choices of  $(D_1, D_2)$  that give rise to smaller values of  $d(D_1, D_2|p)$  could be reasonable estimates of  $(\widehat{D}_1, \widehat{D}_2)$ . To help visualise which  $(D_1, D_2)$  parameter pairs lead to a close match with the synthetic data we use an indicator function

$$\mathcal{I}_1(D_1, D_2|p, \varepsilon) = \begin{cases} 1, & \text{if } d(D_1, D_2|p) \leq \varepsilon, \\ 0, & \text{otherwise.} \end{cases} \quad (2.20)$$

The indicator function is unity if the discrepancy is smaller than some specified threshold,  $\varepsilon$ , and zero elsewhere. Plotting  $\mathcal{I}_1(D_1, D_2|p, \varepsilon)$  as a function of  $(D_1, D_2)$  is a useful way to visualise which combinations of  $(D_1, D_2)$  lead to good matches between  $T(p, t)$  and  $\widehat{T}(p, t)$ . Plots of  $\mathcal{I}_1(D_1, D_2|p, \varepsilon)$  as a function of  $(D_1, D_2)$  are constructed by discretising the  $(D_1, D_2)$  parameter space using a fine square mesh, and evaluating  $\mathcal{I}_1(D_1, D_2|p, \varepsilon)$  at each point on the mesh for various choices of  $\varepsilon$ . All results presented in this work use a fine mesh of  $2001 \times 2001$  equally-spaced values of  $D_1$  and  $D_2$ . Each time we sweep across the parameter space we evaluate the solutions of Equations (2.11)-(2.18) more than 4 million times. Therefore, it is vitally important that the method we use to solve the governing equations is both accurate and efficient.

Results in Figure 2.3 show the region of  $(D_1, D_2)$  parameter space where  $\mathcal{I}_1(D_1, D_2|l_2, \varepsilon) = 1$  for  $\varepsilon = 0.5, 1.0$  and  $1.5$ . Regardless of our choice of  $\varepsilon$ , we see that there are multiple combinations of  $(D_1, D_2)$  for which the time series,  $T(p, t)$ , is very close to the synthetic time series,  $\widehat{T}(p, t)$ . As  $\varepsilon$  decreases, the area for which  $\mathcal{I}_1(D_1, D_2|l_2, \varepsilon) = 1$  decreases, as the discrepancy measure is more restrictive. However, even with further reductions in  $\varepsilon > 0$ , we still observe a very large number of  $(D_1, D_2)$  pairs at which it is very difficult, if not impossible, to reliably distinguish between  $\widehat{T}(p, t)$  and  $T(p, t)$ . This result indicates that relying solely upon Cuttle's experimental protocol may not allow us to reliably identify unique choices of  $(D_1, D_2)$ . We note that reducing the tolerance to zero,  $\varepsilon = 0$ , means that the region in  $(D_1, D_2)$  parameter space where  $\mathcal{I}_1(D_1, D_2|l_2, \varepsilon) = 1$  does shrink

to a unique point. However, working with a zero tolerance is impractical as we wish to allow for a small positive tolerance to account for some variability in the experimental measurements. Furthermore, working with a zero tolerance on a discretised parameter space is impractical since any regular meshing of the  $(D_1, D_2)$  parameter space would not precisely coincide with  $(\hat{D}_1, \hat{D}_2)$ .




---

Figure 2.3: Regions of bounded parameter space where  $\mathcal{I}_1(D_1, D_2|l_2, \varepsilon) = 1$ , for  $l_1 = 1.6$  mm and  $l_2 = 4$  mm. The black circle indicates the target parameters,  $(\hat{D}_1, \hat{D}_2)$ . We plot  $\mathcal{I}_1(D_1, D_2|l_2, \varepsilon)$  on the bounded region  $D_1^{(\min)} \leq D_1 \leq D_1^{(\max)}$  and  $D_2^{(\min)} \leq D_2 \leq D_2^{(\max)}$ , where  $D_1^{(\min)} = \hat{D}_1/20$ ,  $D_1^{(\max)} = 5\hat{D}_1$ ,  $D_2^{(\min)} = \hat{D}_2/20$  and  $D_2^{(\max)} = 5\hat{D}_2$ . The coloured regions satisfy  $\mathcal{I}_1(D_1, D_2|l_2, \varepsilon) = 1$  for  $\varepsilon = 0.5$  (green), 1.0 (red) and 1.5 (blue). The central inset shows a magnified region, identified by the dashed rectangle in the main Figure, about the target parameter pair. The right-most inset indicates the geometry of the skin layers with the brown circle showing the location of the probe,  $p = l_2$ .

---

While the plot of  $\mathcal{I}_1(D_1, D_2|l_2, \varepsilon)$  in Figure 2.3 is shown on the bounded region,  $\hat{D}_1/20 \leq D_1 \leq 5\hat{D}_1$  and  $\hat{D}_2/20 \leq D_2 \leq 5\hat{D}_2$ , we also generated additional results by plotting  $\mathcal{I}_1(D_1, D_2|l_2, \varepsilon)$  over a larger support. These additional results (not shown) indi-

cate that increasing the support leads to further choices of  $(D_1, D_2)$  pairs for which  $T(p, t)$  is very difficult to distinguish from  $\widehat{T}(p, t)$ . That is, the extent of the coloured regions in Figure 2.3 continue to expand as the  $(D_1, D_2)$  support increases. This observation further corroborates our notion that it can be very difficult to infer  $(D_1, D_2)$ , using a single probe located at  $p = l_2$  (Simpson et al., 2017), and this observation motivates us to consider whether different choices of  $p$  could alter our ability to estimate  $(D_1, D_2)$ .

### 2.3.2 Parameter inference: optimal placement of single probe

All results in Section 2.3.1 follow Cuttle's experimental protocol by considering a single probe placed at  $p = l_2$ . Therefore, we now repeat the process of generating the data in the same format as Figure 2.3 but for difference choices of probe location,  $p$ . To first explore the role of  $p$  we assume that some reasonable alternative choices to place the probe are:

1. the centre of the skin layer,  $p = l_1/2$ ,
2. the layer interface,  $p = l_1$ ;
3. the centre of the two-layer system,  $p = l_2/2$ ; and
4. the centre of the fat layer,  $p = l_1 + (l_2 - l_1)/2$ .

Results in Figure 2.4 show plots that are equivalent to Figure 2.3 except that we consider these four different choices of  $p$ . Comparing data in Figures 2.3-2.4 shows that the choice of  $p$  has a dramatic impact upon the sensitivity of our ability to distinguish between  $T(p, t)$  and  $\widehat{T}(p, t)$ . Perhaps the most obvious result is that choosing  $p = l_1/2$ , as in Figure 2.4(a), leads to a very poor ability to estimate  $(D_1, D_2)$  since the extent of the coloured region is very large. This result makes intuitive sense because placing a single probe in the skin layer provides very little direct information about  $D_2$ . In contrast, placing the probe at the centre of the two-layer system,  $p = l_1 + (l_2 - l_1)/2$ , as in Figure 2.4(c), provides a better opportunity to estimate  $(D_1, D_2)$  since the extent of the coloured regions are smallest compared to the other choices of  $p$  in Figures 2.3-2.4. Overall, it appears to be optimal to place the probe in the fat layer, rather than the skin layer. This is a useful outcome as it is consistent with Cuttle's experimental protocol (Cuttle et al., 2006, 2008a,b, 2010).

All discussion of the results in Figures 2.3-2.4 are so far based on qualitative visual interpretations of the extent of the coloured regions in these plots. To provide more quantitative insight we introduce a metric

$$\mathcal{A}_1 = \frac{1}{A} \int_{D_2^{(\min)}}^{D_2^{(\max)}} \int_{D_1^{(\min)}}^{D_1^{(\max)}} \mathcal{I}_1 \, dD_1 \, dD_2, \quad (2.21)$$

where  $A = (D_1^{(\max)} - D_1^{(\min)}) \times (D_2^{(\max)} - D_2^{(\min)})$  is the total area of the bounded parameter space in Figures 2.3-2.4. Here,  $\mathcal{A}_1$  is the proportion of the bounded parameter space where the indicator function is unity when we consider data collected at a single probe. Although we write  $\mathcal{A}_1$  in terms of a double integral in Equation (2.21), we find it simplest to interpret  $\mathcal{A}_1$  as the proportion of the parameter space in which the indicator function is unity. Therefore, we estimate  $\mathcal{A}_1$  by calculating  $\mathcal{I}_1$  at each point on the discretised  $(D_1, D_2)$  parameter space and computing the proportion of the  $2001^2$  evaluations of  $\mathcal{I}_1$  that are unity. To interpret these results we note that smaller values of  $\mathcal{A}_1$  are associated with improved experimental designs since the region of parameter space where  $T(p, t)$  is a close match to  $\widehat{T}(p, t)$  is reduced when  $\mathcal{A}_1$  is smaller. Plotting  $\mathcal{A}_1$  as a function of  $p$  in Figure 2.5 gives us greater quantitative insight into the role of probe placement.

Results in Figure 2.5 show that  $\mathcal{A}_1$  appears to decrease with  $p$  for all values of  $\varepsilon$  we consider. The data in Figure 2.5 is useful because it provides a quantitative framework for examining the importance of the choice of probe placement,  $p$ . Overall we see that larger values of  $p$  lead to improved experimental designs, and we see that once  $p > 1.8$  mm that  $\mathcal{A}_1$  becomes relatively insensitive to any further increase in  $p$ . A simple recommendation we can provide from this exploration is that placing a single probe into the fat layer is a good experimental design.

All results presented in this study so far focus on the case where temperature data is recorded at a single location,  $x = p$ . While this constraint is an important feature of Cuttle's experimental protocol (Cuttle et al., 2006, 2008a,b, 2010), our mathematical modelling tools give us the flexibility to quantitatively explore the benefit of collecting data at more than one location in a controlled manner that is not possible experimentally. Therefore, we will now consider how our ability to estimate  $(D_1, D_2)$  are influenced if we were able to collect temperature data at two locations,  $x = p$  and  $x = q$ .

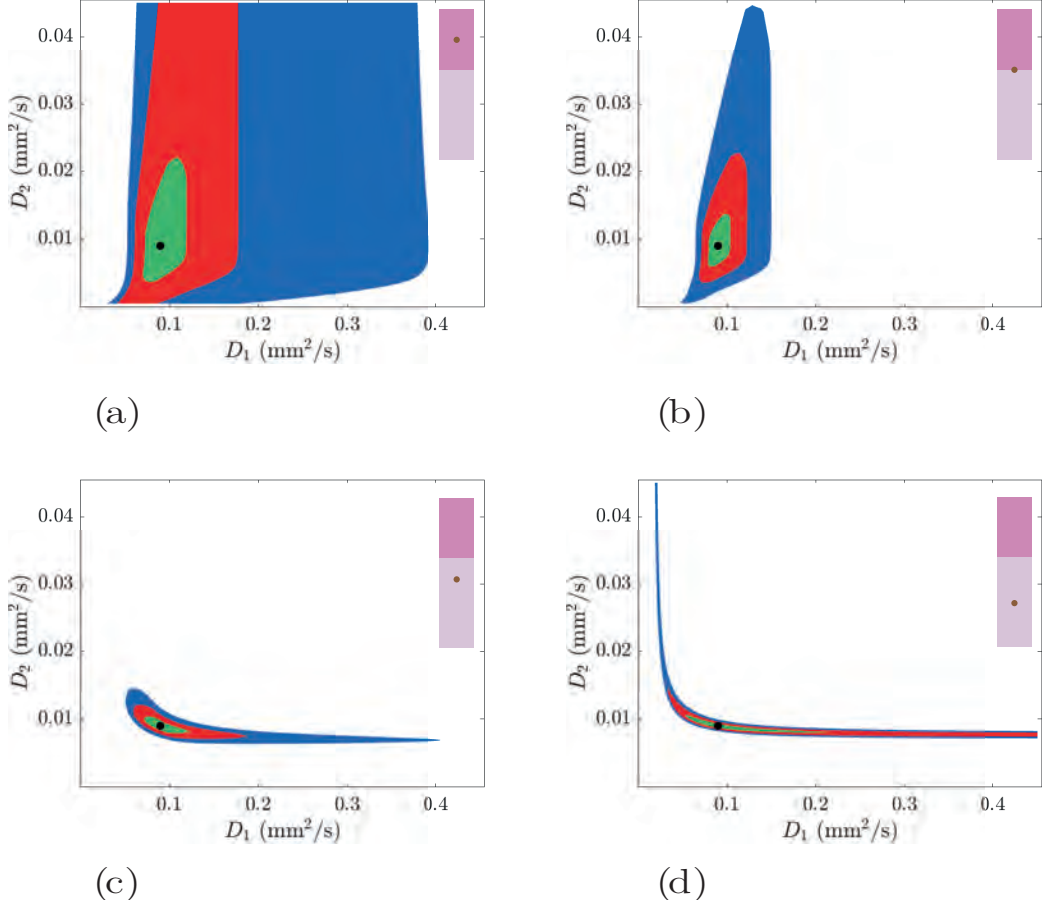


Figure 2.4: The role of probe location,  $p$ . As in Figure 2.3 the target parameter pair,  $(\hat{D}_1, \hat{D}_2)$ , is highlighted with a black circle and the insets show various experimental designs with the brown circles showing the probe location relative to the tissue geometry. In each subfigure, the coloured regions satisfy  $\mathcal{I}_1(D_1, D_2|p, \varepsilon) = 1$  for  $\varepsilon = 0.5$  (green), 1.0 (red) and 1.5 (blue). **(a)** Probe at the centre of the skin layer,  $p = l_1/2$ ; **(b)** Probe at the layer interface,  $p = l_1$ ; **(c)** Probe at the centre of the two-layer system,  $p = l_2/2$ ; **(d)** Probe at the centre of the fat layer,  $p = l_1 + (l_2 - l_1)/2$ . In all cases we set  $l_1 = 1.6$  mm and  $l_2 = 4$  mm.

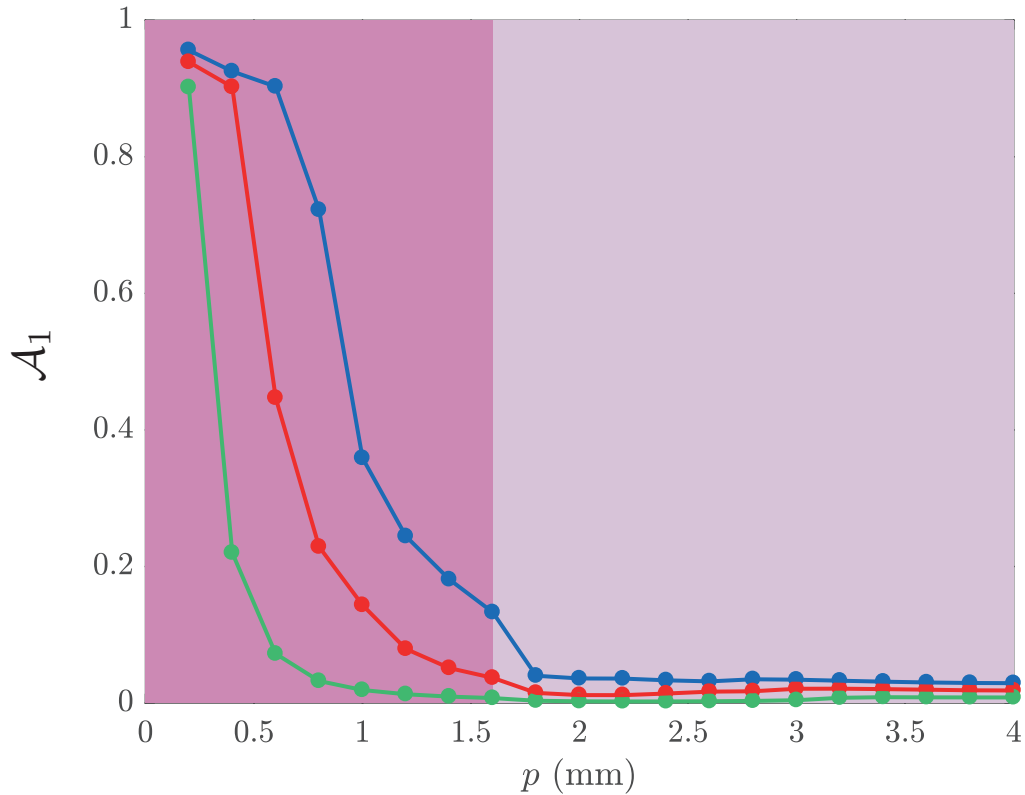


Figure 2.5: The influence of probe location,  $p$ , on  $\mathcal{A}_1$  for  $\widehat{D}_1/20 \leq D_1 \leq 5\widehat{D}_1$  and  $\widehat{D}_2/20 \leq D_2 \leq 5\widehat{D}_2$ , and  $l_1 = 1.6$  mm and  $l_2 = 4$  mm. Plots of  $\mathcal{A}_1$  are shown for  $\varepsilon = 0.5$  (green),  $\varepsilon = 1.0$  (red) and  $\varepsilon = 1.5$  (blue). Calculations are performed for 20 equally-spaced values of  $p$ , from  $p = 0.2$  mm to  $p = 4$  mm. The bright pink and lighter pink background colours are chosen to correspond with the colour of the skin and fat layers in Figure 2.1(b).

### 2.3.3 Parameter inference: two probes

To keep the presentation of our results manageable, when we consider the case where data is collected at two locations,  $x = p$  and  $x = q$ , we restrict our attention to the subset of cases where the location of the first probe,  $x = p$ , is fixed at  $p = l_2$  as in Cuttle's experiments (Cuttle et al., 2006, 2008a,b, 2010). With this constraint, we then focus on how we might choose the location of the second probe,  $x = q$ . To achieve this we modify our definition of the indicator function to be

$$\mathcal{I}_2(D_1, D_2|p, q, \varepsilon) = \begin{cases} 1, & \text{if } d(D_1, D_2|p) \leq \varepsilon \text{ and } d(D_1, D_2|q) \leq \varepsilon, \\ 0, & \text{otherwise,} \end{cases} \quad (2.22)$$

where  $d(D_1, D_2|q)$  is defined in exactly the same way as  $d(D_1, D_2|p)$  except that the spatial location is different. The key difference between  $\mathcal{I}_1$  and  $\mathcal{I}_2$  is that  $\mathcal{I}_2$  measures the closeness of  $T(x, t)$  and  $\widehat{T}(x, t)$  at both  $x = p$  and  $x = q$ , whereas  $\mathcal{I}_1$  measures the closeness of  $T(x, t)$  and  $\widehat{T}(x, t)$  at  $x = p$  only. We follow our previous approach from Section 2.3.2 by proposing four sensible choices for the placement of the second probe:

1. the centre of the skin layer,  $q = l_1/2$ ;
2. the layer interface,  $q = l_1$ ;
3. the centre of the two-layer system,  $q = l_2/2$ ; and
4. the centre of the fat layer,  $q = l_1 + (l_2 - l_1)/2$ .

Results in Figure 2.6 show plots of the regions where  $\mathcal{I}_2(D_1, D_2|l_2, q, \varepsilon) = 1$ . The arrangement of the subfigures in Figure 2.6 corresponds to the arrangement of the subfigures in Figure 2.4 except that we now have two probes in the layered system. Comparing the extent of the coloured regions where  $\mathcal{I}_2(D_1, D_2|l_2, q, \varepsilon) = 1$  in Figure 2.6 to the extent of the colored regions where  $\mathcal{I}_1(D_1, D_2|l_2, \varepsilon) = 1$  in Figure 2.4 provides information about how the collection of additional data at a second location would improve our ability to reliably distinguish between  $T(x, t)$  and  $\widehat{T}(x, t)$  at  $x = l_2$  only (Figure 2.4), compared to our ability to distinguish between  $T(x, t)$  and  $\widehat{T}(x, t)$  at both  $x = l_2$  and  $x = q$  (Figure 2.6). Overall, regardless of the choice of  $q$ , we see that working with a second probe always reduces the extent of the coloured region. Furthermore, comparing results across the four subfigures in Figure 2.6 indicates that the configuration in Figure 2.6(b), where the second probe is placed at the layer interface  $x = l_1$ , is the best configuration of these four possibilities since the extent of the coloured regions is smallest.

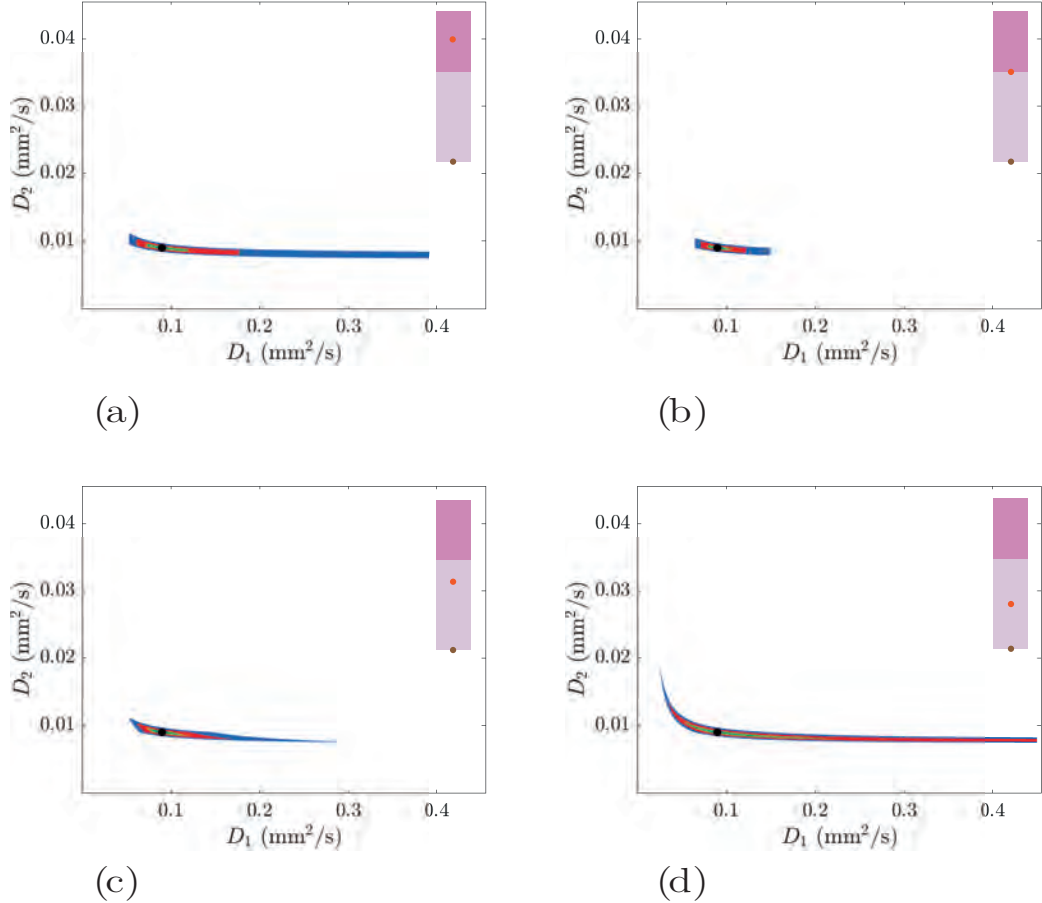


Figure 2.6: The role of the second probe location,  $q$ . As with Figure 2.4 the target parameter pair,  $(\hat{D}_1, \hat{D}_2)$ , is highlighted with a black circle and the insets show various experimental designs with the brown circles showing the fixed first probe location and the red circles showing the variable second probe location relative to the tissue geometry. In each subfigure, the coloured regions satisfy  $\mathcal{I}_2(D_1, D_2 | l_1, l_2, q, \varepsilon) = 1$  for  $\varepsilon = 0.5$  (green), 1.0 (red) and 1.5 (blue). (a) Second probe at the centre of the skin layer,  $q = l_1/2$ ; (b) Second probe at the layer interface,  $q = l_1$ ; (c) Second probe at the centre of the two-layer system,  $q = l_2/2$ ; (d) Second probe at the centre of the fat layer,  $p = l_1 + (l_2 - l_1)/2$ . In all results we set  $l_1 = 1.6$  mm and  $l_2 = 4$  mm.

### 2.3.4 Parameter inference: optimal placement of second probe

To extend the results in Figure 2.6, we now explore whether there is some optimal placement of the second probe. To explore this question we introduce

$$\mathcal{A}_2 = \frac{1}{A} \int_{D_2^{(\min)}}^{D_2^{(\max)}} \int_{D_1^{(\min)}}^{D_1^{(\max)}} \mathcal{I}_2 \, dD_1 dD_2, \quad (2.23)$$

where  $\mathcal{A}_2$  is the proportion of the parameter space that satisfies  $\mathcal{I}_2(D_1, D_2 | l_2, q, \varepsilon) = 1$ . Similar to our approach in Section 2.3.2, we seek to find  $q$  which minimises  $\mathcal{A}_2$ .

Results in Figure 2.7 show  $\mathcal{A}_2$  as a function of  $q$ , for different choices of  $\varepsilon$ . Remarkably, we see that setting  $q = 1.6$  mm minimises  $\mathcal{A}_2$ , for all  $\varepsilon$  considered. This results implies that the optimal location for a second probe, given that a first probe is already located at the bottom of the fat tissue  $p = l_2$ , is at or near the layer interface,  $q = l_1$ .

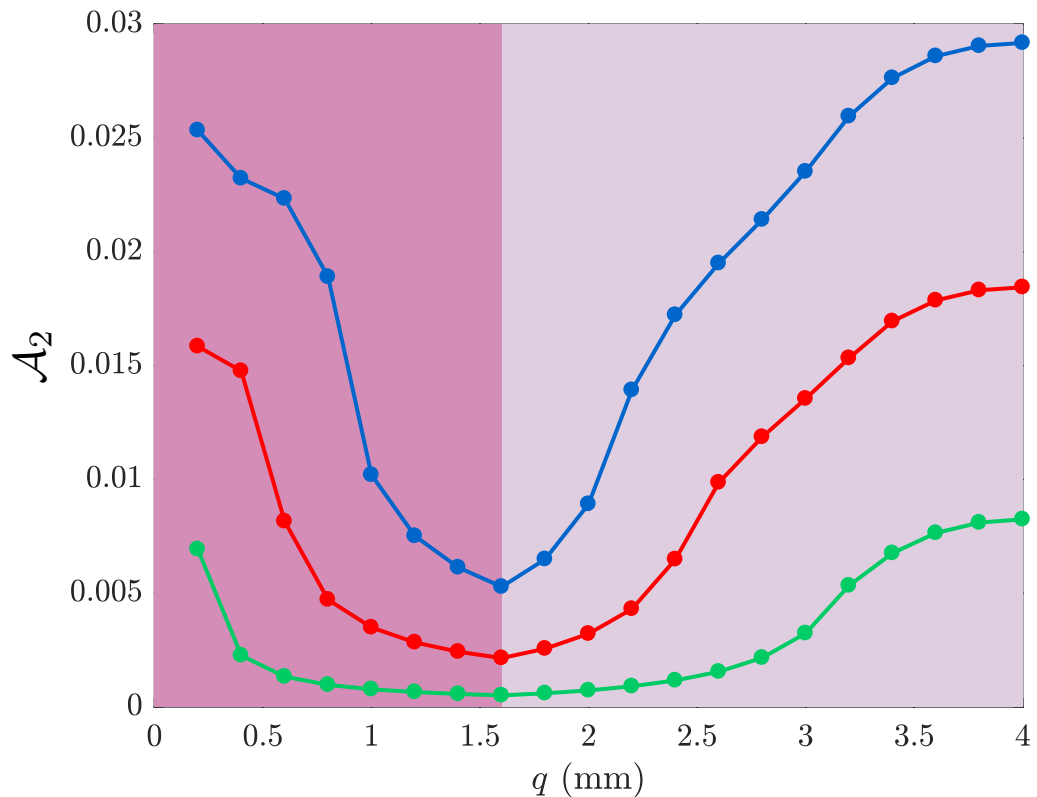


Figure 2.7: The influence of the second probe location,  $q$ , on  $\mathcal{A}_2$  for  $\hat{D}_1/20 \leq D_1 \leq 5\hat{D}_1$  and  $\hat{D}_2/20 \leq D_2 \leq 5\hat{D}_2$ , and  $l_1 = 1.6$  mm and  $l_2 = 4$  mm. Plots of  $\mathcal{A}_2$  are shown for  $\varepsilon = 0.5$  (green),  $\varepsilon = 1.0$  (red) and  $\varepsilon = 1.5$  (blue). In all cases  $p = l_2$  and calculations are performed for 20 equally-spaced values of  $q$  from  $q = 0.2$  mm to  $q = 4$  mm. The bright pink and lighter pink background colours are chosen to correspond with the colour of the skin and fat layers in Figure 2.1(b).

## 2.4 Conclusions and future directions

In this work we consider an experiential protocol designed by Cuttle and co-workers (Cuttle et al., 2006, 2008a,b, 2010) to quantify the conduction of heat in living porcine (pig) tissues. This unique experimental protocol is very important because many experimental studies that examine heat conduction in skin tissue focus on non-living excised tissues (Henriques and Moritz, 1947; Moritz and Henriques, 1947; El-Brawany et al., 2009; Brown et al., 1993) whereas the protocol developed by Cuttle is far more realistic because they deal with living tissues, *in situ*. One of the constraints of Cuttle's experimental protocol is that the temperature within the living tissues is monitored using a subdermal probe at a single location within the layered skin. Because skin is a layered structure, with the epidermis and dermis layers overlying a deeper fat layer, it is natural for us to model the conduction of heat in this system using a heterogeneous multilayer model where the thermal diffusivity in each layer can be different. In this work we idealise the skin tissues as a two-layer system with the upper layer representing the epidermis and dermis combined, and the lower layer representing the subdermal fat. Since one of the main biological functions of the fat layer is to provide thermal insulation (Hayward and Keatinge, 1981), we expect that the thermal diffusivity of the fat layer to be different to the thermal diffusivity of the skin layer.

The key question we address in this work is to explore whether temperature data at a single location in a two-layer system is sufficient for us to reliably estimate the thermal diffusivity in the skin and fat layers,  $(D_1, D_2)$ . Using biologically-motivated target values,  $(\hat{D}_1, \hat{D}_2)$ , we solve the two-layer model and convert the spatiotemporal solution into a simple time series at a single location. This data is compatible with the kind of data recorded and reported by Cuttle and colleagues (Cuttle et al., 2006, 2008a,b, 2010). We then systematically scan the  $(D_1, D_2)$  parameter space, solving the model over four million parameter pairs, to explore the extent to which this time series data can be used to reliably identify the target parameters,  $(\hat{D}_1, \hat{D}_2)$ . Our results show that our ability to estimate the parameters can be very sensitive using this kind of data as there are many combinations of parameter pairs,  $(D_1, D_2)$ , leading to virtually indistinguishable time series data at a single location. Once we have demonstrated this sensitivity, we then explore the question of experimental design by using the mathematical model to explore the extent to which our ability to estimate  $(D_1, D_2)$  depends on the depth at which the subdermal probe is placed. In summary, we find that it is best to place the probe in the fat layer. This result is reassuring since Cuttle's experimental protocol places the probe at the bottom of the fat

layer Cuttle et al. (2006, 2008a,b, 2010). We conclude by exploring the extent to which our ability to estimate  $(D_1, D_2)$  improves if we consider the case where two subdermal probes, placed at different locations, are used. Our results show that using a second probe always improves our ability to estimate  $(D_1, D_2)$ , but there is still some sensitivity in terms of the placement of the subdermal probes. In summary, if it were possible to use two subdermal proves we find that given the first probe is placed at the bottom of the fat layer, and second probe ought to be placed at the interface of the skin and fat layers.

There are many ways that our study could be extended since we have invoked several simplifications and assumptions that could be relaxed. A key assumption in our work is that we treat the synthetic data generated by the mathematical model,  $\widehat{T}(p, t)$  and  $\widehat{T}(q, t)$ , as being deterministic. This means that we neglect the role of experimental variability which is known to be important when dealing with biological data Jin et al. (2017); Warne et al. (2017). If we had an estimate of the experimental variability in Cuttle's measurements, we could incorporate this into our parameter sensitivity analysis by adding an appropriate noise signal, such as white noise, to  $\widehat{T}(p, t)$  and  $\widehat{T}(q, t)$ , and then exploring how the incorporation of experimental variability influences our ability to estimate  $(D_1, D_2)$ . Another feature of our mathematical model that could be explored further is our assumption that the boundary between the bottom of the fat layer and the underlying muscle and bone tissues, at  $x = l_2$  is perfectly insulating. In reality, we expect that there would be some transfer of heat from the fat tissues into the underlying muscle and bone, and this could be incorporated into the model using a Robin boundary condition. This approach would introduce an additional unknown heat transfer coefficient, thereby increasing the dimensionality of the parameter space to be explored. Both of these extensions could be considered in future studies.

Another natural extension of our current work would be to treat the conduction of heat in living skin as a three-layer problem instead of a two-layer problem. The three-layer problem could be constructed by treating the epidermis, dermis and fat as three distinct layers. While the semi-analytical solution strategy for solving the two-layer model generalises perfectly well to a three-layer model, the challenge of identifying three values of the thermal diffusivity instead of two values would become even more challenging when dealing with experimental observations where temperature is recorded at a single location in the layered system. Given that the main result of the current work highlights how challenging it can be to estimate parameters for a two-layer model, we anticipate that it is presently infeasible to meaningfully interpret data from Cuttle's current experimental protocol using a three-layer model. However, if some of the current experimental constraints were to be alleviated and it became feasible to collect experimental temperature data at multiple positions simultaneously, then it is possible that working with a three-layer model

could be reasonable in the future.



## **Chapter 3**

# **Mathematical techniques for continuum models of heat transfer in heterogeneous living skin**

This chapter comprises the supplementary text of the following manuscript:

S McInerney, EJ Carr and MJ Simpson, Parameterising continuum models of heat transfer in heterogeneous living skin using experimental data, *International Journal of Heat and Mass Transfer*, accepted for publication, September 2018.



### 3.1 Mathematical model

Here we briefly recall the mathematical model from the main document. In summary, we consider heat transfer in living skin tissues, which we conceptualise as being composed of two heterogeneous layers: the upper skin layer, and the lower fat layer. We assume that the temporal and spatial distribution of non-dimensional temperature in skin,  $T_1(x, t) \in [0, 1]$ , and in fat,  $T_2(x, t) \in [0, 1]$ , is governed by,

$$\frac{\partial T_1(x, t)}{\partial t} = D_1 \frac{\partial^2 T_1(x, t)}{\partial x^2}, \quad 0 < x < l_1, \quad (3.1)$$

$$\frac{\partial T_2(x, t)}{\partial t} = D_2 \frac{\partial^2 T_2(x, t)}{\partial x^2}, \quad l_1 < x < l_2. \quad (3.2)$$

Equations (3.1)-(3.2) are subject to initial conditions

$$T_1(x, 0) = 0, \quad (3.3)$$

$$T_2(x, 0) = 0, \quad (3.4)$$

and boundary conditions

$$T_1(0, t) = 1, \quad (3.5)$$

$$\frac{\partial T_2(l_2, t)}{\partial x} = 0. \quad (3.6)$$

To close the problem, we also specify two conditions at the interface,  $x = l_1$ ,

$$T_1(l_1, t) = T_2(l_1, t), \quad (3.7)$$

$$D_1 \frac{\partial T_1(l_1, t)}{\partial x} = D_2 \frac{\partial T_2(l_1, t)}{\partial x}. \quad (3.8)$$

Here, Equation (3.7) ensures that the temperature is continuous at the interface, and Equation (3.8) ensures that the flux of thermal energy is continuous at the interface.

Equations (3.1)-(3.8) specify a two-layer thermal diffusion problem, with perfect contact at the layer interface (Carr and Turner, 2016). The initial non-dimensional temperature profile is uniformly zero, and a Dirichlet boundary condition at  $x = 0$  (Equation 3.5) introduces thermal energy into the system into the upper skin layer. A homogeneous Neumann boundary condition at  $x = l_2$  (Equation 3.6) prevents thermal energy from leaving the domain at the base of the fat layer (Simpson et al., 2017). This two-layer model with these boundary conditions implies that perfusion of heat to the blood is negligible and

that the loss of heat through the lower layer at  $x = l_2$  is negligible. It is insightful to note that our choice of boundary conditions means that the long-time steady state solution of the model satisfies

$$\lim_{t \rightarrow \infty} T_1(x, t) = 1, \quad (3.9)$$

$$\lim_{t \rightarrow \infty} T_2(x, t) = 1. \quad (3.10)$$

## 3.2 Model solution

We solve Equations (3.1)-(3.8) using a Laplace transform approach (Carr and Turner, 2016; Debnath and Bhatta, 2007; Rodrigo and Worthy, 2016). We find that it is advantageous to work with a Laplace transform solution, rather than working with numerical solutions, since the Laplace transform solution can be repeatedly evaluated, at very little computational overhead, for any value of  $l_1$  and  $l_2$ . In contrast, if we were to consider varying  $l_1$  or  $l_2$  in a standard numerical algorithm based on a finite volume, finite difference or finite element discretisation of the governing equations we would have to consider re-meshing the problem for different choices of  $l_1$  or  $l_2$ .

The first step in the solution strategy is to introduce an unknown function of time,  $g(t)$ , which acts to uncouple the heat transfer processes in the skin and fat layers. To achieve this, we define

$$g(t) = D_1 \frac{\partial T_1(l_1, t)}{\partial x} = D_2 \frac{\partial T_2(l_1, t)}{\partial x}. \quad (3.11)$$

With this definition, the mathematical description of the heat transfer process in the skin layer can now be written as

$$\frac{\partial T_1(x, t)}{\partial t} = D_1 \frac{\partial^2 T_1(x, t)}{\partial x^2}, \quad 0 < x < l_1, \quad (3.12)$$

$$T_1(x, 0) = 0, \quad (3.13)$$

$$T_1(0, t) = 1, \quad (3.14)$$

$$D_1 \frac{\partial T_1(l_1, t)}{\partial x} = g(t). \quad (3.15)$$

The mathematical description of the heat transfer process in the fat layer can now be

written as

$$\frac{\partial T_2(x, t)}{\partial t} = D_2 \frac{\partial^2 T_2(x, t)}{\partial x^2}, \quad l_1 < x < l_2, \quad (3.16)$$

$$T_2(x, 0) = 0, \quad (3.17)$$

$$D_2 \frac{\partial T_2(l_1, t)}{\partial x} = g(t), \quad (3.18)$$

$$\frac{\partial T_2(l_2, t)}{\partial x} = 0, \quad (3.19)$$

with  $g(t)$  to be determined.

In this work we denote the Laplace transform of  $f(t)$  as

$$\bar{f}(s) = \int_0^\infty e^{-st} f(t) dt, \quad (3.20)$$

where  $s$  is chosen such that the improper integral converges (Debnath and Bhatta, 2007). Taking the Laplace transform of Equations (3.12)-(3.15) with respect to  $t$ , we obtain

$$D_1 \frac{d^2 \bar{T}_1(x|s)}{dx^2} = s \bar{T}_1(x|s), \quad 0 < x < l_1, \quad (3.21)$$

$$\bar{T}_1(0|s) = \frac{1}{s}, \quad (3.22)$$

$$D_1 \frac{d\bar{T}_1(l_1|s)}{dx} = \bar{g}(s), \quad (3.23)$$

where we use the notation  $\bar{T}_1(x|s)$  to denote the Laplace transform of  $T_1(x, t)$ . This notation makes it clear that  $\bar{T}_1(x|s)$  depends upon  $x$ , and that we treat the Laplace transform variable as a constant parameter. Similarly, taking the Laplace transform of Equations (3.16)-(3.19), we obtain

$$D_2 \frac{d^2 \bar{T}_2(x|s)}{dx^2} = s \bar{T}_2(x|s), \quad l_1 < x < l_2, \quad (3.24)$$

$$D_2 \frac{d\bar{T}_2(l_1|s)}{dx} = \bar{g}(s), \quad (3.25)$$

$$\frac{d\bar{T}_2(l_2|s)}{dx} = 0. \quad (3.26)$$

The general solutions of Equation (3.21) and Equation (3.24) are given by

$$\bar{T}_1(x|s) = A_1 e^{\xi_1 x} + B_1 e^{-\xi_1 x}, \quad 0 < x < l_1, \quad (3.27)$$

$$\bar{T}_2(x|s) = A_2 e^{\xi_2 x} + B_2 e^{-\xi_2 x}, \quad l_1 < x < l_2, \quad (3.28)$$

where  $\xi_1 = \sqrt{s/D_1}$  and  $\xi_2 = \sqrt{s/D_2}$ . To determine  $A_1$  and  $B_1$ , we enforce the boundary

conditions given by Equations (3.22)-(3.23), resulting in

$$A_1 + B_1 = \frac{1}{s}, \quad (3.29)$$

$$A_1 e^{\xi_1 l_1} - B_1 e^{-\xi_1 l_1} = \frac{\bar{g}(s)}{D_1 \xi_1}. \quad (3.30)$$

Equations (3.29)-(3.30) form a linear system for  $A_1$  and  $B_1$ , and the solution of this system gives

$$A_1 = \frac{D_1 \xi_1 e^{-\xi_1 l_1} + s \bar{g}(s)}{2s D_1 \xi_1 \cosh(\xi_1 l_1)}, \quad (3.31)$$

$$B_1 = \frac{D_1 \xi_1 e^{\xi_1 l_1} - s \bar{g}(s)}{2s D_1 \xi_1 \cosh(\xi_1 l_1)}. \quad (3.32)$$

Combining Equations (3.27), (3.31) and (3.32) we have

$$\bar{T}_1(x|s) = \frac{\cosh(\xi_1[x - l_1])}{s \cosh(\xi_1 l_1)} + \frac{\sinh(\xi_1 x)}{D_1 \xi_1 \cosh(\xi_1 l_1)} \bar{g}(s). \quad (3.33)$$

Following a similar procedure we can enforce boundary conditions, given by Equations (3.25)-(3.26), to obtain a linear system involving  $A_2$  and  $B_2$ . Solving this linear system, and substituting the expressions for these constants into Equation (3.28) gives

$$A_2 = \frac{-\bar{g}(s) e^{-\xi_2 l_2}}{2D_2 \xi_2 \sinh(\xi_2 [l_2 - l_1])}, \quad (3.34)$$

$$B_2 = \frac{-\bar{g}(s) e^{\xi_2 l_2}}{2D_2 \xi_2 \sinh(\xi_2 [l_2 - l_1])}, \quad (3.35)$$

$$\bar{T}_2(x|s) = \frac{-\cosh(\xi_2[l_2 - x])}{D_2 \xi_2 \sinh(\xi_2 [l_2 - l_1])} \bar{g}(s). \quad (3.36)$$

Both Equations (3.33) and (3.36) depend upon  $\bar{g}(s)$ , which is unknown at present. To determine  $\bar{g}(s)$ , we take the Laplace transform of Equation (3.7), which gives

$$\bar{T}_1(l_1|s) = \bar{T}_2(l_1|s). \quad (3.37)$$

Substituting Equation (3.33) and Equation (3.36) into Equation (3.37), and re-arranging the resulting expression allows  $\bar{g}(s)$  to be determined

$$\bar{g}(s) = \frac{-D_1 \xi_1 D_2 \xi_2 \tanh(\xi_2 [l_2 - l_1])}{s \cosh(\xi_1 l_1) [D_2 \xi_2 \tanh(\xi_1 l_1) \tanh(\xi_2 [l_2 - l_1]) + D_1 \xi_1]}. \quad (3.38)$$

Finally, substituting the expression for  $\bar{g}(s)$  into Equations (3.33) and (3.36) yields

$$\bar{T}_1(x|s) = \frac{\cosh(\xi_1[x - l_1])}{s \cosh(\xi_1 l_1)} - \frac{D_2 \xi_2 \sinh(\xi_1 x) \tanh(\xi_2[l_2 - l_1])}{s \cosh^2(\xi_1 l_1) [D_2 \xi_2 \tanh(\xi_1 l_1) \tanh(\xi_2[l_2 - l_1]) + D_1 \xi_1]}, \quad (3.39)$$

$$\bar{T}_2(x|s) = \frac{D_1 \xi_1 \cosh(\xi_2[x - l_2]) \tanh(\xi_2[l_2 - l_1])}{s \cosh(\xi_1 l_1) \sinh(\xi_2[l_2 - l_1]) [D_2 \xi_2 \tanh(\xi_1 l_1) \tanh(\xi_2[l_2 - l_1]) + D_1 \xi_1]}. \quad (3.40)$$

Given our expressions for  $\bar{T}_1(x|s)$  and  $\bar{T}_2(x|s)$ , we seek to take the inverse Laplace transform to give  $T_1(x, t)$  and  $T_2(x, t)$ , respectively. Simply attempting to take the inverse Laplace transforms of Equations (3.39)-(3.40) using standard symbolic software does not give a closed-form solution for  $T_1(x, t)$  and  $T_2(x, t)$ . Therefore, we evaluate the inverse Laplace transform numerically (Hoog et al., 1982; Simpson and Ellery, 2014). To achieve this we use the algorithm described by Trefethen and colleagues (Trefethen et al., 2006). Since we use a numerical method to invert the Laplace transform expressions we refer to our solution method as a *semi-analytical* method Carr and Turner (2016). To verify the accuracy of our semi-analytical solution, we also solve the mathematical model numerically and visually compare the numerical and semi-analytical solutions over a range of parameter choices in Section 3.4.

### 3.3 Numerical solution

We now describe a finite volume scheme that we use to solve Equations (3.1)-(3.7) numerically. We intend to use these numerical solutions to verify the accuracy of the semi-analytical solution presented in Section 3.2. The numerical method involves discretising the domain with a spatially-uniform mesh consisting of  $N$  equally-spaced nodes. Adjacent nodes are separated by a distance  $\Delta x$ . A vertex-centered finite volume approximation is adopted (Ozisik, 1968), with control volume faces positioned at the midpoint between adjacent nodes. We choose  $\Delta x$  so that the  $K^{\text{th}}$  node is located at the layer interface. The details of the finite volume mesh are given in Figure 3.1.

To describe the numerical method, we let  $T_{1,i}^{(j)}$  and  $T_{2,i}^{(j)}$  denote the numerical approximations of  $T_1(x_i, t_j)$  and  $T_2(x_i, t_j)$ , respectively. We first consider a control volume at an interior node that is not at the interface, and integrate Equations (3.1)-(3.2) over the control volume. The integrals of the spatial derivative terms associated with the terms on the right of Equations (3.1)-(3.2) are evaluated using the fundamental theorem of calculus. The integrals of the temporal derivative terms associated with the left side of Equations (3.1)-(3.2) are evaluated by first taking the temporal derivative outside of the integral

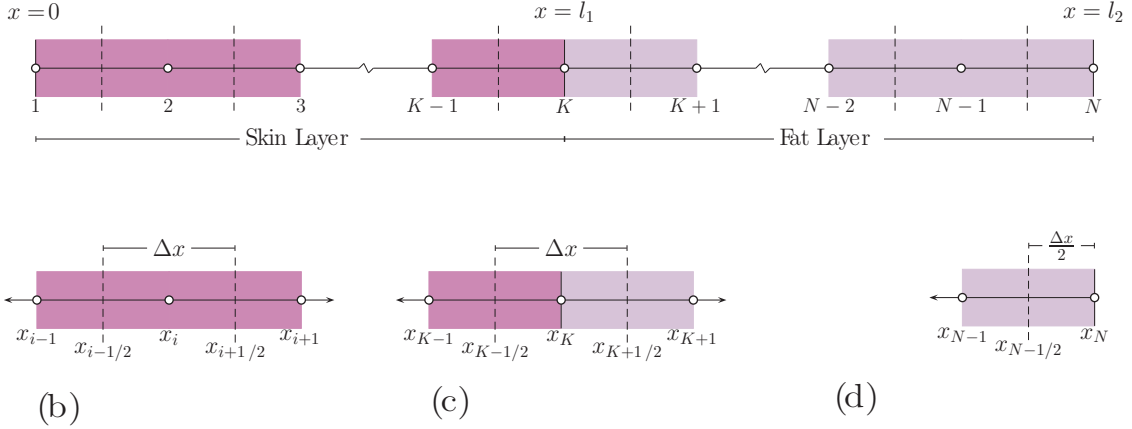


Figure 3.1: (a) Finite volume discretisation with  $N$  nodes, with  $\Delta x$  chosen so that the  $K^{\text{th}}$  node is located at the interface,  $x = l_1$ . Vertical dashed lines indicate the control volume faces, and the node numbering and spatial location of nodes are as indicated. (b) Control volume associated with the  $i^{\text{th}}$  node in the skin layer. The location of the node is denoted  $x_i$ , and nearest neighbour nodes are located at  $x_{i\pm 1}$ . The locations of the control volume faces are denoted  $x_{i\pm 1/2}$ , as indicated. The distance between the interior control volume faces is  $\Delta x$ . (c) Control volume associated with the  $K^{\text{th}}$  node at the interface. At  $x_{K-1/2}$  the thermal diffusivity is  $D_1$ , and at  $x_{K+1/2}$  the thermal diffusivity is  $D_2$ . (d) Control volume associated with the  $N^{\text{th}}$  node, showing that the distance between the two faces of this control volume is  $\Delta x/2$ . The bright pink and lighter pink background colours are chosen to correspond with the colour of the skin and fat layers in Figure 2.1(b).

expressions, and then evaluating the resulting integral using the midpoint rule, giving

$$\Delta x \frac{dT_{1,i}}{dt} = D_1 \left[ \frac{\partial T_1(x_{i+1/2}, t)}{\partial x} - \frac{\partial T_1(x_{i-1/2}, t)}{\partial x} \right], \quad 2 \leq i \leq K-1, \quad (3.41)$$

$$\Delta x \frac{dT_{2,i}}{dt} = D_2 \left[ \frac{\partial T_2(x_{i+1/2}, t)}{\partial x} - \frac{\partial T_2(x_{i-1/2}, t)}{\partial x} \right], \quad K+1 \leq i \leq N-1. \quad (3.42)$$

Approximating the spatial derivatives at the control volume faces in Equations (3.41)-(3.42) using a central difference approximation gives

$$\Delta x \frac{dT_{1,i}}{dt} = \frac{D_1}{\Delta x} [T_{1,i-1} - 2T_{1,i} + T_{1,i+1}], \quad 2 \leq i \leq K-1, \quad (3.43)$$

$$\Delta x \frac{dT_{2,i}}{dt} = \frac{D_2}{\Delta x} [T_{2,i-1} - 2T_{2,i} + T_{2,i+1}], \quad K+1 \leq i \leq N-1, \quad (3.44)$$

where we have made use of the fact that we are dealing with a spatially uniform mesh.

We now integrate Equations (3.43)-(3.44) through time, from  $t_j$  to time  $t_{j+1}$ , where

$t_{j+1} = t_j + \Delta t$ . For simplicity we adopt a forward Euler approximation so that the terms on the right of Equations (3.43)-(3.44) are evaluated at  $t_j$ , giving

$$T_{1,i}^{(j+1)} = T_{1,i}^{(j)} + \frac{D_1 \Delta t}{(\Delta x)^2} [T_{1,i-1}^{(j)} - 2T_{1,i}^{(j)} + T_{1,i+1}^{(j)}], \quad 2 \leq i \leq K-1 \quad (3.45)$$

$$T_{2,i}^{(j+1)} = T_{2,i}^{(j)} + \frac{D_2 \Delta t}{(\Delta x)^2} [T_{2,i-1}^{(j)} - 2T_{2,i}^{(j)} + T_{2,i+1}^{(j)}], \quad K+1 \leq i \leq N-1. \quad (3.46)$$

To specify the initial conditions, given by Equations (3.3)-(3.4), we set

$$T_{1,i}^{(0)} = 0, \quad 2 \leq i \leq K, \quad (3.47)$$

$$T_{2,i}^{(0)} = 0, \quad K+1 \leq i \leq N. \quad (3.48)$$

To specify the boundary condition at  $x = 0$ , given by Equation (3.5), we set

$$T_{1,1}^{(j)} = 1. \quad (3.49)$$

Greater care must be taken to specify the boundary condition at  $x = l_2$ . Unlike the rest of the control volumes, the width of the control volume around the  $N^{\text{th}}$  node is  $\Delta x/2$  and the right face of this control volume is at  $x_N$ , as illustrated in Figure 3.1(d). Integrating Equation (3.2) from  $x_{N-1/2}$  to  $x_N$ , and following the same procedure to evaluate the integrals used previously when dealing with the interior nodes, we obtain

$$\frac{\Delta x}{2} \frac{dT_{2,N}}{dt} = D_2 \left[ \frac{\partial T_2(x_N, t)}{\partial x} - \frac{\partial T_2(x_{N-1/2}, t)}{\partial x} \right]. \quad (3.50)$$

The boundary condition at  $x = l_2$ , or node  $x_N$ , given by Equation (3.6), can be implemented by setting the first term on the right in Equation (3.50) to zero. If we then evaluate the remaining spatial derivative term in Equation (3.50) using a central difference approximation at the control volume face we obtain

$$\frac{\Delta x}{2} \frac{dT_{2,N}}{dt} = \frac{D_2}{\Delta x} [T_{2,N-1} - T_{2,N}]. \quad (3.51)$$

Integrating Equation (3.51) through time using the same forward Euler approximation used at the interior nodes gives

$$T_{2,N}^{(j+1)} = T_{2,N}^{(j)} + \frac{2D_2 \Delta t}{(\Delta x)^2} [T_{2,N-1}^{(j)} - T_{2,N}^{(j)}]. \quad (3.52)$$

The  $K^{\text{th}}$  node at the interface of the two layers is treated slightly differently to the other interior nodes. The spatially-integrated analogue of Equations (3.41)-(3.42) at the

$K^{\text{th}}$  node is

$$\Delta x \frac{dT_{1,K}}{dt} = \left[ D_2 \frac{\partial T_2(x_{K+1/2}, t)}{\partial x} - D_1 \frac{\partial T_1(x_{K-1/2}, t)}{\partial x} \right], \quad (3.53)$$

where we have diffusivity  $D_1$  at the left face of the control volume and diffusivity  $D_2$  at the right face of the control volume. Note that  $T_{1,K} = T_{2,K}$  due to Equation (3.7) so that we do not need to consider a separate control volume for  $T_{2,K}$ . Approximating the spatial derivative terms in Equation (3.53) using a central difference approximation gives

$$\Delta x \frac{dT_{1,K}}{dt} = \frac{1}{\Delta x} [D_1 T_{1,K-1} - (D_1 + D_2) T_{1,K} + D_2 T_{2,K+1}], \quad (3.54)$$

where again we make use of the fact that we are dealing with a spatially uniform mesh. We integrate Equation (3.54) through time using the same forward Euler approximation used at the interior nodes, giving

$$T_{1,K}^{(j+1)} = T_{1,K}^{(j)} + \frac{\Delta t}{(\Delta x)^2} \left[ D_1 T_{1,K-1}^{(j)} - (D_1 + D_2) T_{1,K}^{(j)} + D_2 T_{2,K+1}^{(j)} \right]. \quad (3.55)$$

In summary, our numerical scheme is given by Equations (3.45)-(3.49) and Equation (3.55). Together, these equations can be processed efficiently in matrix form, which we summarise as

$$\mathbf{T}^{(j+1)} = \mathbf{T}^{(j)} + \frac{\Delta t}{(\Delta x)^2} \mathbf{A} \mathbf{T}^{(j)}, \quad (3.56)$$

where  $\mathbf{T}^{(j)} = [T_{1,1}^{(j)}, T_{1,2}^{(j)}, \dots, T_{1,K}^{(j)}, T_{2,K+1}^{(j)}, \dots, T_{2,N-1}^{(j)}, T_{2,N}^{(j)}]^T$  and  $\mathbf{A}$  is a tridiagonal matrix. When we implement the numerical solution we store  $\mathbf{A}$  in vector form. Denoting the lower diagonal, main diagonal and upper diagonal of  $\mathbf{A}$  as  $\mathbf{A}_L$ ,  $\mathbf{A}_D$  and  $\mathbf{A}_U$ , respectively, we have

$$\mathbf{A}_L = [D_1, \dots, D_1, D_1, D_2, \dots, D_2, 2D_2]^T, \quad (3.57)$$

$$\mathbf{A}_D = [0, -2D_1, \dots, -2D_1, -(D_1 + D_2), -2D_2, \dots, -2D_2, -2D_2]^T, \quad (3.58)$$

$$\mathbf{A}_U = [0, D_1, \dots, D_1, D_2, D_2, \dots, D_2]^T. \quad (3.59)$$

### 3.4 Solution verification

We now apply the semi-analytical solution technique from Section 3.2 and the numerical solution technique from Section 3.3 to a suite of four test problems. A visual comparison of the semi-analytical and numerical solutions will serve as a test of the accuracy of the

semi-analytical solution. Results for four particular test cases are shown in Figure 3.2, where the semi-analytical solution is superimposed on the numerical solution. In these four test cases we hold  $l_2$  constant, and we vary the location of the interface,  $l_1$ . Similarly we hold the diffusivity in the fat layer,  $D_2$  to be constant, and we vary the diffusivity in the skin layer,  $D_1$ . Results in Figure S2 show that the initial temperature is zero at all locations. For  $t > 0$ , the temperature at  $x = 0$  is unity and we see that thermal energy propagates into the skin layer and across the interface into the fat layer. It is of interest to note that the solution profile is continuous at the interface, but that the slope of the solution is discontinuous at the interface. The discontinuity in the slope of the solution is particularly pronounced in Figure 3.2(c) where the difference in  $D_1$  and  $D_2$  is most pronounced. Importantly, the main result here is that the semi-analytical solution is visually indistinguishable from the numerical solution, at this scale, for all four test cases.

It is worthwhile to note that the solutions associated with each test case in Figure 3.2 are plotted at six different values of time. However, the values of time chosen in each subfigure are different. Since we vary  $l_1$  and  $D_1$  in each test case, we expect that each test case will require a different duration of time to effectively asymptote to the steady state solution, where  $\lim_{t \rightarrow \infty} T_1(x, t) = \lim_{t \rightarrow \infty} T_2(x, t) = 1$ . To deal with this, for each test case we first calculate an estimate of the critical time,  $t_c$  (Landman and McGuinness, 2000; Carr, 2017; Carr and Simpson, 2018). In this work we take the critical time to be the time at which the temperature at  $x = l_2$  reaches within 1% of the steady value. That is, we calculate  $t_c$  that satisfies  $T_2(l_2, t_c) = 0.99$ , and we note that this value is different for the four test cases shown in Figure 3.2. In particular we have  $t_c = 2.7, 1.3, 0.6$  and  $9.7$  s for the four test cases in Figure 3.2(a)-(d), respectively. Given this information we then calculate the numerical and semi-analytical solutions at six different values of time:  $t = 0.01t_c, 0.05t_c, 0.1t_c, 0.25t_c, 0.5t_c$  and  $t_c$ .

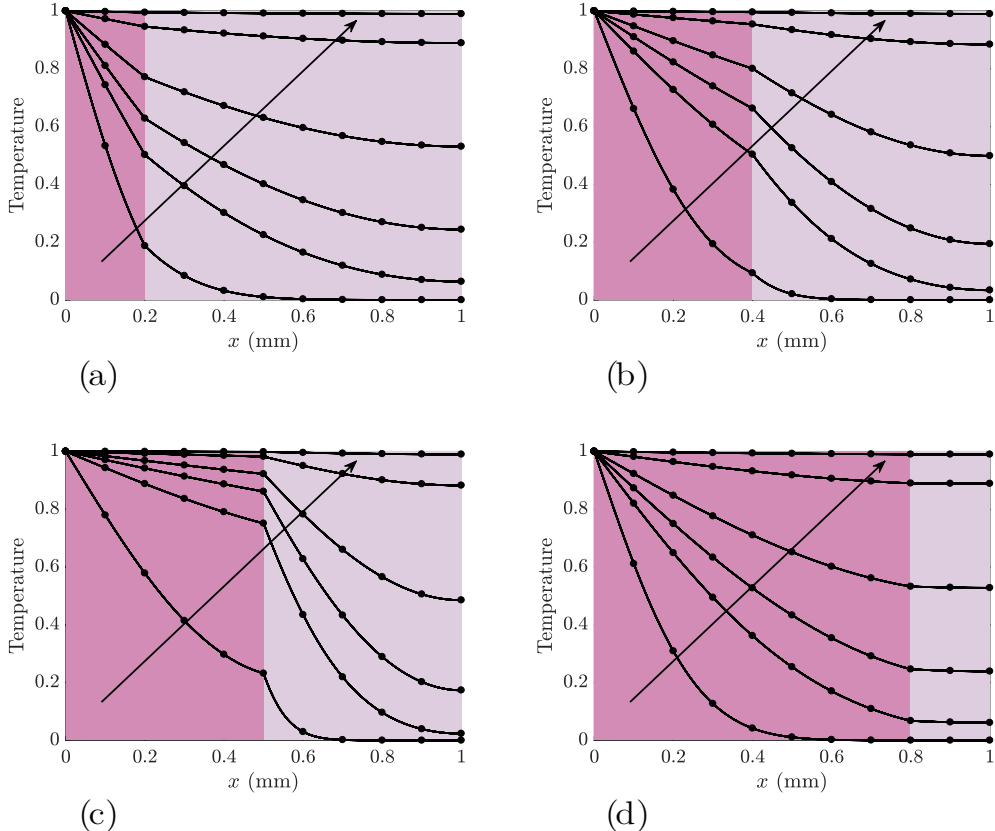


Figure 3.2: Comparison of semi-analytical (lines) and numerical (dots) solutions to Equations (3.1)-(3.8). The arrows indicate the direction of increasing time. In all four test cases we set  $D_2 = 1 \text{ mm}^2/\text{s}$  and  $l_2 = 1 \text{ mm}$ . Other parameter values are: (a)  $D_1 = 0.5 \text{ mm}^2/\text{s}$  and  $l_1 = 0.2 \text{ mm}$ ; (b)  $D_1 = 2 \text{ mm}^2/\text{s}$  and  $l_1 = 0.4 \text{ mm}$ ; (c)  $D_1 = 10 \text{ mm}^2/\text{s}$  and  $l_1 = 0.5 \text{ mm}$ ; and (d)  $D_1 = 0.2 \text{ mm}^2/\text{s}$  and  $l_1 = 0.8 \text{ mm}$ . Numerical solutions are obtained with  $\Delta t = 10^{-6}t_c \text{ s}$  and  $\Delta x = 0.005 \text{ mm}$ , giving a mesh of 201 nodes. The numerical solutions are shown at every 20<sup>th</sup> spatial node, and at times corresponding to  $t = 0.01t_c, 0.05t_c, 0.1t_c, 0.25t_c, 0.5t_c$  and  $t_c$ . The background colours are chosen to correspond with Figure 2.1(b).





# Chapter 4

## Conclusions

### 4.1 Summary and Discussion

This thesis proposes a continuum model of heat transfer in heterogeneous living skin, explores the difficulty of the parameter inference process in such a model with spatially limited experimental data and outlines a solution methodology for the mathematical model. By expanding our knowledge of heat transfer in skin tissue, we are better able to understand burn injuries.

In this study, we develop a mathematical model to analyse heat conduction experiments on *in vivo* porcine skin tissue. The model incorporates the layered structure of the tissue, by defining a skin layer and a fat layer, each with distinct thermal diffusivities describing heat transfer within the respective layers,  $(D_1, D_2)$ . A notable limitation of the heat conduction experiments is that all data is extracted from a single subdermal temperature probe. This motivates us to investigate whether the inference of the two thermal diffusivity parameters is possible with data from a single location and how experimental design could improve this parameter inference process. To reduce the number of influencing factors in this investigation, we then generate synthetic experimental data to mimic the *in vivo* porcine experiments. This data is obtained by evaluating the solution of our two-layer mathematical model at a single location at regular time intervals using biologically-motivated target parameter values,  $(\hat{D}_1, \hat{D}_2)$ . We seek to accurately infer the target parameter values using only the generated time-series data. This is done by methodically evaluating the solution of the mathematical model for over four million parameter pairs and testing the discrepancy between the evaluated solution and the synthetic data. If the evaluated solution is sufficiently close to the data, according to some threshold discrepancy, we consider the parameter pair that generates that solution to be acceptable estimates of the target parameter pair. A large number of such parameter pairs

would imply that the parameter inference process was imprecise, whereas a small number would imply precision.

We find that the accurate inference of the thermal diffusivities of skin and fat in our simplified two-layer diffusion model is impossible using the experimental temperature data extracted from a single probe, regardless of the probe location. We also find that, if limited to the use of a single probe, placing the probe in the fat layer is preferable to the skin layer, in terms of improving precision of parameter inference. We then investigate how the use of a second probe could improve the accuracy of the parameter estimation. We find that if the first probe is fixed at the bottom of the fat layer, the optimal location for the second probe is the layer interface, again in terms of accurately inferring the thermal diffusivities of skin and fat. With this experimental configuration, the two parameters can be approximated with a relatively high level of precision. These findings could be used in the future to inform experimentalists who wish to obtain accurate estimates of the parameters in a system modelled using a layered heat transfer model.

To complement the work performed exploring the parameter inference process of our mathematical model, we also outline and verify the accuracy of the solution methodology for the model. The particular solution methodology we implement was presented recently in the literature (Carr and Turner, 2016; Rodrigo and Worthy, 2016) and utilises what is referred to as a semi-analytical approach. Comparing the accuracy against a numerical scheme, we found this approach offers an accurate solution for a low computational cost. The semi-analytical solution can be extended to more sophisticated models with relative ease.

## 4.2 Directions for Future Research

A notable limitation of the work presented in this thesis is that the findings are confined to one particular layered heat transfer model of a particular spatial structure. Future research may look at extending this investigation to alternative models; for example, to models that have more than two layers or to models that do not assume perfect thermal insulation at the bottom of the fat layer. By using a model with two layers, we obscure some of the nuances of the tissue structure. In particular, the skin layer comprises an epidermis layer and a dermis layer, each with different physical properties. In a three-layer model without the imposition of thermal insulation at the bottom of the system, the temporal and spatial distribution of the temperature in each of the layers,  $T_1(x, t)$ ,

$T_2(x, t)$  and  $T_3(x, t)$ , can be described by,

$$\frac{\partial T_1(x, t)}{\partial t} = D_1 \frac{\partial^2 T_1(x, t)}{\partial x^2}, \quad 0 < x < l_1, \quad (4.1)$$

$$\frac{\partial T_2(x, t)}{\partial t} = D_2 \frac{\partial^2 T_2(x, t)}{\partial x^2}, \quad l_1 < x < l_2, \quad (4.2)$$

$$\frac{\partial T_3(x, t)}{\partial t} = D_3 \frac{\partial^2 T_3(x, t)}{\partial x^2}, \quad l_2 < x < l_3, \quad (4.3)$$

for  $t > 0$ , subject to initial conditions

$$T_1(x, 0) = 0, \quad (4.4)$$

$$T_2(x, 0) = 0, \quad (4.5)$$

$$T_3(x, 0) = 0, \quad (4.6)$$

boundary conditions

$$T_1(0, t) = 1, \quad (4.7)$$

$$\frac{\partial T_3(l_3, t)}{\partial x} = -\gamma T_3(l_3, t), \quad (4.8)$$

and conditions at the layer interfaces

$$T_1(l_1, t) = T_2(l_1, t), \quad (4.9)$$

$$D_1 \frac{\partial T_1(l_1, t)}{\partial x} = D_2 \frac{\partial T_2(l_1, t)}{\partial x}, \quad (4.10)$$

$$T_2(l_2, t) = T_3(l_2, t), \quad (4.11)$$

$$D_2 \frac{\partial T_2(l_2, t)}{\partial x} = D_3 \frac{\partial T_3(l_2, t)}{\partial x}. \quad (4.12)$$

where  $D_1$ ,  $D_2$  and  $D_3$  are the unknown thermal diffusivities in each layer,  $l_1$ ,  $l_2$  and  $l_3$  are the known depths of the layers and  $\gamma$  is an unknown heat transfer coefficient governing the rate at which thermal energy is lost at the bottom of the system. A three-layer model provides a better representation of the tissue than a two-layer model, as the three layers accounts for the epidermis, dermis and fat separately, but introduces one more unknown parameter,  $D_3$ . This modification to the model makes precise parameter inference more complicated. Similarly, by allowing the loss of heat from the system at  $x = l_3$ , our model becomes more indicative of the process we are modelling, but at the cost of introducing another parameter,  $\gamma$ . An exploration could be undertaken to determine the number of probes required to infer the four unknown parameters in this new model and the optimal location of the probes. Earlier in this thesis, we found that two probes placed at  $x = l_1$  and

$x = l_2$  allowed for accurate approximations of the two unknown parameters in the two-layer model. For a three-layer model with four unknown parameters, how many probes would be necessary? It may be the case that three probes at  $x = l_1$ ,  $x = l_2$  and  $x = l_3$  would be sufficient: one for each layer. That would certainly be a reasonable guess in the case where  $\gamma$  is known and the task is to infer just  $D_1$ ,  $D_2$  and  $D_3$ , but does the introduction of a fourth unknown parameter demand the use of a fourth probe in order to estimate all the parameters accurately? To perform this investigation, the new model would have to be solved and modifications would need to be made to the code provided in the Appendix. An additional complication of this exploration is the visualisation of a four-dimensional parameter space.

Another possible avenue of future research is an investigation into the robustness of our findings under the variation of the spatial structure of the tissue. That is to say, are the optimal single probe and two probe configurations consistent for systems where the widths of the layers vary? All findings in this thesis are based on a single spatial structure: a skin layer from 0 mm to 1.6 mm and a fat layer from 1.6 mm to 4 mm. We find that if limited to a single probe, placing the probe in the fat layer is preferable to placing it in the skin layer, but would this be the case if the skin layer is much thicker than the fat layer? Also, we find that if the first probe was placed at the bottom of the system, a second probe at the layer interface allows for precise parameter inference, but is this true when the location of the layer interface is varied? The algorithms provided in this thesis could be used to answer these questions, with only minor modifications.

It is my hope that this thesis is able to provide a framework for future investigations into the parameter inference process of a variety of layered heat transfer models.





# Bibliography

- A Abdullahi, S Amini-Nik, and M Jeschke. Animal models in burn research. *Cellular and Molecular Life Sciences*, 71:3241–3255, 2014.
- CJ Andrews, L Cuttle, and MJ Simpson. Quantifying the role of burn temperature, burn duration and skin thickness in an *in vivo* animal skin model of heat conduction. *International Journal of Heat and Mass Transfer*, 101:542–549, 2016.
- A Baldwin, J Xu, and D Attinger. How to cool a burn: a heat transfer point of view. *Journal of Burn Care & Research*, 33:176–187, 2012.
- SM Brown, ML Baesso, J Shen, and RD Snook. Thermal diffusivity of skin measured by two photothermal techniques. *Analytica Chimica Acta*, 282:711–719, 1993.
- EJ Carr. Calculating how long it takes for a diffusion process to effectively reach steady state without computing the transient solution. *Physical Review E*, 96:012116, 2017.
- EJ Carr and MJ Simpson. Accurate and efficient calculation of response times for ground-water flow. *Journal of Hydrology*, 558:470–481, 2018.
- EJ Carr and IW Turner. A semi-analytical solution for multilayer diffusion in a composite medium consisting of a large number of layers. *Applied Mathematical Modelling*, 40: 7034–7050, 2016.
- EJ Carr, IW Turner, and P Perré. Macroscale modelling of multilayer diffusion: Using volume averaging to correct the boundary conditions. *Applied Mathematical Modelling*, 47:600–618, 2017.
- L Cuttle, M Kempf, GE Phillips, J Mill, MT Hayes, JF Fraser, X-Q Wang, and RM Kimble. A porcine deep dermal partial thickness burn model with hypertrophic scarring. *Burns*, 32:806–820, 2006.
- L Cuttle, M Kempf, O Kravchuk, N George, P-Y Liu, H-E Chang, J Mill, X-Q Wang, and RM Kimble. The efficacy of aloe vera, tea tree oil and saliva as first aid treatment for partial thickness burn injuries. *Burns*, 34:1176–1182, 2008a.

- L Cuttle, M Kempf, O Kravchuk, GE Phillips, J Mill, X-Q Wang, and RM Kimble. The optimal temperature of first aid treatment for partial thickness burn injuries. *Wound Repair and Regeneration*, 16:626–634, 2008b.
- L Cuttle, M Kempf, P-Y Liu, O Kravchuk, and RM Kimble. The optimal duration and delay of first aid treatment for deep partial thickness burn injuries. *Burns*, 36:673–679, 2010.
- L Debnath and D Bhatta. *Integral transforms and their applications*. Chapman and Hall, Boca Raton, 2007.
- KR Diller, LJ Hayes, and GK Blake. Analysis of alternate models for simulating thermal burns. *Journal of Burn Care & Research*, 12:177–189, 1991.
- MA El-Bawany, DK Nassiri, G Terhaar, A Shaw, I Rivens, and K Lozhken. Measurement of thermal and ultrasonic properties of some biological tissues. *Journal of Medical Engineering & Technology*, 33:249–256, 2009.
- P Haridas, JA McGovern, DLS McElwain, and MJ Simpson. Quantitative comparison of the spreading and invasion of radial growth phase and metastatic melanoma cells in a three-dimensional human skin equivalent model. *PeerJ*, 5:e3754, 2017.
- P Haridas, AP Browning, JA McGovern, DLS McElwain, and MJ Simpson. Three-dimensional experiments and individual based simulations show that cell proliferation drives melanoma nest formation in human skin tissue. *BMC Systems Biology*, 12:34, 2018.
- MG Hayward and WR Keatinge. Roles of subcutaneous fat and thermoregulatory reflexes in determining ability to stabilize body temperature in water. *The Journal of Physiology*, 320:229–251, 1981.
- FC Henriques and AR Moritz. Studies of thermal injury: I. the conduction of heat to and through skin and the temperatures attained therein. a theoretical and an experimental investigation. *The American Journal of Pathology*, 23:530–549, 1947.
- RI Hickson, SI Barry, and GN Mercer. Critical times in multilayer diffusion. part 1: Exact solutions. *International Journal of Heat and Mass Transfer*, 52:5776–5783, 2009a.
- RI Hickson, SI Barry, and GN Mercer. Critical times in multilayer diffusion. part 2: Approximate solution. *International Journal of Heat and Mass Transfer*, 52:5784–5791, 2009b.

- FR De Hoog, JH Knight, and AN Stokes. An improved method for numerical inversion of laplace transforms. *SIAM Journal on Scientific and Statistical Computing*, 3:357–366, 1982.
- W Jin, ET Shah, CJ Penington, SW McCue, PK Maini, and MJ Simpson. Logistic proliferation of cells in scratch assays is delayed. *Bulletin of Mathematical Biology*, 79: 1028–1050, 2017.
- ME Johnson, D Blankschtein, and R Langer. Evaluation of solute permeation through the stratum corneum: Lateral bilayer diffusion as the primary transport mechanism. *Journal of Pharmaceutical Sciences*, 86:1162–1172, 1997.
- E Kengne and A Lakhssassi. Bioheat transfer problem for one-dimensional spherical biological tissues. *Mathematical Biosciences*, 269:1–9, 2015.
- KA Landman and MA McGuinness. Mean action time for diffusive processes. *Journal of Applied Mathematics and Decision Sciences*, 4:125–141, 2000.
- H Li. Epidemiology and outcome analysis of 6325 burn patients: a five-year retrospective study in a major burn center in southwest china. *Scientific Reports*, 7:46966, 2017.
- GN Mercer and HS Sidhu. A heat transfer model describing burns to the skin from automotive airbags. *The ANZIAM Journal*, 47:339–354, 2006.
- W Meyer, R Schwarz, and K Neurand. The skin of domestic mammals as a model for the human skin, with special reference to the domestic pig. *Current Problems in Dermatology*, 7:39–52, 1978.
- W Montagna and JS Yun. The skin of the domestic pig. *Journal of Investigative Dermatology*, 41:11–21, 1964.
- AR Moritz and FC Henriques. Studies of thermal injury: II. the relative importance of time and surface temperature in the causation of cutaneous burns. *The American Journal of Pathology*, 23:695–720, 1947.
- DP Orgill, MG Solari, MS Barlow, and NE OConnor. A finite-element model predicts thermal damage in cutaneous contact burns. *Journal of Burn Care & Research*, 19: 203–209, 1998.
- C Orndorff, S Ponomarev, W Dai, and A Bejan. Thermal analysis in a triple-layered skin structure with embedded vasculature, tumor, and gold nanoshells. *International Journal of Heat and Mass Transfer*, 111:677–695, 2017.

- MN Ozisik. *Boundary value problems of heat conduction*. International Textbook Company, Scranton, Pennsylvania, 1968.
- HH Pennes. Analysis of tissue and arterial blood temperatures in the resting human forearm. *Journal of Applied Physiology*, 1:93–122, 1948.
- MR Rodrigo and A Worthy. Solution of multilayer diffusion problems via the laplace transform. *Journal of Mathematical Analysis and Applications*, 444:475–502, 2016.
- D Sarker, A Haji-Sheikh, and A Jain. Temperature distribution in multi-layer skin tissue in presence of a tumor. *International Journal of Heat and Mass Transfer*, 91:602–610, 2015.
- N Sheils. Multilayer diffusion in a composite medium with imperfect contact. *Applied Mathematical Modelling*, 46:450–464, 2017.
- N Sheils and B Deconinck. Heat conduction on the ring: Interface problems with periodic boundary conditions. *Applied Mathematics Letters*, 37:107–11, 2014.
- RL Sheridan. *Burns: A practical approach to immediate treatment and long-term care*. Manson Publishing, London, 2012.
- MJ Simpson. Depth-averaging errors in reactive transport modeling. *Water Resources Research*, 45:1–8, 2009.
- MJ Simpson. Critical time scales for morphogen gradient formation: Concentration or gradient criteria? *International Journal of Heat and Mass Transfer*, 106:570–572, 2017.
- MJ Simpson and AJ Ellery. Exact series solutions of reactive transport models with general initial conditions. *Journal of Hydrology*, 513:7–12, 2014.
- MJ Simpson, S McInerney, EJ Carr, and L Cuttle. Quantifying the efficacy of first aid treatments for burn injuries using mathematical modelling and *in vivo* porcine experiments. *Scientific Reports*, 7:10925, 2017.
- TP Sullivan, WH Eaglstein, SC Davis, and P Mertz. The pig as a model for human wound healing. *Wound Repair and Regeneration*, 9:66–76, 2001.
- LN Trefethen, JAC Weideman, and T Schmelzer. Talbot quadratures and rational approximations. *BIT Numerical Mathematics*, 46:653–670, 2006.
- D van der Merwe, JD Brooks, R Gehring, RE Baynes, NA Monteiro-Riviere, and JE Riviere. A physiologically based pharmacokinetic model of ogranophosphate dermal absorption. *Toxicological Science*, 89:188–204, 2006.

DJ Warne, RE Baker, and MJ Simpson. Optimal quantification of contact inhibition in cell populations. *Biophysical Journal*, 113:1920–1924, 2017.

FM Wood, M Phillips, T Jovic, JT Cassidy, P Cameron, and DW Edgar. Water first aid is beneficial in humans post-burn: evidence from a bi-national cohort study. *PLOS ONE*, 11:e0147259, 2016.



# Appendix

Appended to this thesis are the MATLAB functions and scripts used to solve and analyse the mathematical models presented throughout the document. This code is also available at GitHub (<https://github.com/seanmcinerneyQUT/Thesis>).

## Model\_Solve.m

This function is used to evaluate the solution to the mathematical model presented in Equations (2.11)-(2.18). It requires the use of two other functions. It requires Laplace\_Temperature.m, which formulates a solution to the equations after a Laplace transform has been performed. It then uses cf.m, which takes a numerical inverse Laplace algorithm to obtain the solution to the original equations. Model\_Solve.m could be used for different one-dimensional mathematical models, as long as Laplace\_Temperature.m is updated appropriately.

```
function T = Model_Solve( x , t , D1 , D2 , L1 , L2 )
% Author: Sean McInerney; Last Update: 17/05/2018
% Solves a two layer diffusion problem, given x, t and appropriate
% model parameters. Uses numerical inverse Laplace code, cf.m, on an
% analytical Laplace solution to the problem, as formulated in
% Laplace_Temperature.m
%
% Solution to Equations (2.11)-(2.18)
%
% FUNCTION INPUTS:
% x - Depth
% t - Time
% D1 - Diffusivity in skin layer
% D2 - Diffusivity in fat layer
% L1 - Depth of layer interface
```

```

% L2 - Depth of entire system
% FUNCTION OUTPUT:
% T - Model solution discretised as a matrix [nx by nt]

% Used for inverse Laplace
n = 14;
[z,c] = cf(n);

% Initialise T
N = length(x);
M = length(t);
T = zeros(N,M);

% TBar(S,X) formulates the Laplace solution
TBar = @(S,X) Laplace_Temperature(S,X,D1,D2,L1,L2);
% Loop over space and time
for i = 1:N
    for j = 1:M
        % Check if initial condition needs to be applied
        if t(j) == 0
            T(i,j) = 0;
        else
            % Perform inverse Laplace
            T(i,j) = 0;
            for k = 1:n/2
                I = 2*k-1;
                s = z(I)/t(j);
                T(i,j) = T(i,j) - c(I)*TBar(s,x(i))/t(j);
            end
            T(i,j) = 2*real(T(i,j));
        end
    end
end

end

```

### Laplace\_Temperature.m

This function is used to evaluate the solutions to Equations (3.21)-(3.26), as outlined in Equation (3.39) and Equation (3.40). The function is specific to the mathematical model presented in Equations (3.1)-(3.8). To perform analysis on different mathematical models, which describe different physical mechanisms, Laplace\_Temperature.m would have to be modified.

```

function TBar = Laplace_Temperature( s , x , D1 , D2 , L1 , L2 )
% Author: Sean McInerney; Last Update: 17/05/2018
% Given s and x and the appropriate parameters, Laplace_Temperature returns
% the Laplace solution to the following two-layer thermal diffusion problem
%
% x = 0 ----- T(0,t) = 1
%           standard diffusion according to D1
%           T_1(x,0) = 0
%
% x = L1 ----- thermal flux conserved
%           standard diffusion according to D2
%           T_2(x,0) = 0
%
%
% x = L2 ----- heat insulated
%
% FUNCTION INPUTS:
% s - Laplace variable
% x - Depth
% D1 - Diffusivity in skin layer
% D2 - Diffusivity in fat layer
% L1 - Depth of layer interface
% L2 - Depth of entire system
% FUNCTION OUTPUT:
% TBar - Laplace solution

% Establish intermediate parameters
xi1 = sqrt(s/D1);
xi2 = sqrt(s/D2);

```

```

if x < L1
    % Skin layer solution (Refer to Equation (3.39)_
    TBar = cosh(xi1*(x-L1))/(s*cosh(xi1*L1)) - ...
        (D2*xi2*sinh(xi1*x)*tanh(xi2*(L2-L1))) / ...
        (s*cosh(xi1*L1)^2*(D2*xi2*tanh(xi1*L1)*tanh(xi2*(L2-L1))+D1*xi1));
else
    % Fat layer solution (Refer to Equation (3.40))
    TBar = (D1*xi1*cosh(xi2*(x-L2))*tanh(xi2*(L2-L1))) / ...
        (s*cosh(xi1*L1)*sinh(xi2*(L2-L1))*(D2*xi2*tanh(xi1*L1)*...
        tanh(xi2*(L2-L1))+D1*xi1));
end

end

```

**cf.m**

This function was *not* developed by me. It has been included as it is referred to in other functions and scripts. For further information regarding cf.m, see the paper where the function is first presented (Trefethen et al., 2006).

```

function [zk,ck] = cf(n)
% Computes the poles zk and residues ck by the Caratheodory-Fejer method
% for the type (n,n) best approximation to exp(z) on the negative real
% line.
%
% For full details see:
% J. A. C. Weideman L. N. Trefethen and T. Schmelzer (2006) Talbot
% quadratures and rational approximations. BIT Numer. Math., 46:653-670.
%
% The following code is given in Figure 4.1 of the above paper.

K = 75;                      % no of Cheb coeffs
nf = 1024;                     % no of pts for FFT
w = exp(2i*pi*(0:nf-1)/nf); % roots of unity
t = real(w);                  % Cheb pts (twice over)
scl = 9;                       % scale factor for stability

```

```

F = exp(scl*(t-1)./(t+1+1e-16)); % exp(x) transpl. to [-1,1]
c = real(fft(F))/nf; % Cheb coeffs of F
f = polyval(c(K+1:-1:1),w); % analytic part f of F
[U,S,V] = svd(hankel(c(2:K+1))); % SVD of Hankel matrix
s = S(n+1,n+1); % singular value
u = U(K:-1:1,n+1)'; v = V(:,n+1)'; % singular vector
zz = zeros(1,nf-K); % zeros for padding
b = fft([u zz])./fft([v zz]); % finite Blaschke product
rt = f-s*w.^K.*b; % extended function r-tilde
rtc = real(fft(rt))/nf; % its Laurent coeffs
zr = roots(v); qk = zr(abs(zr)>1); % poles
qc = poly(qk); % coeffs of denominator
pt = rt.*polyval(qc,w); % numerator
ptc = real(fft(pt)/nf); % coeffs of numerator
ptc = ptc(n+1:-1:1); ck = 0*qk;

for k = 1:n % calculate residues
    q = qk(k); q2 = poly(qk(qk~=q));
    ck(k) = polyval(ptc,q)/polyval(q2,q);
end

zk = scl*(qk-1).^2./(qk+1).^2; % poles in z-plane
ck = 4*ck.*zk./((qk.^2-1); % residues in z-plane

```

### TestParameterSpace.m

This function is used to evaluate  $\mathcal{A}_1$  or  $\mathcal{A}_2$  for a given choice of probe location(s), as detailed in Equations (2.21) and (2.23). It requires the use of the functions Model\_Solve.m, Laplace\_Temperature.m and cf.m. This is very computationally expensive if a fine mesh of the parameter space is used to calculate  $\mathcal{A}_1$  and  $\mathcal{A}_2$ .

```

function TestParameterSpace( p , q )
%% Test Parameter Space
% Author: Sean McInerney; Last Update: 18/06/2018
%
% Used to generate Figures 2.3, 2.4 and 2.6
%
% Is computational costly for high values of Npts

```

```

%
% FUNCTION INPUTS:
% p - The first probe location
% q - The second probe location. Input 'none', if no second probe is used

%% Set-up

close all

% Target Parameters
D1_hat = 0.09;
D2_hat = 0.009;

% Spatial Structure
L1 = 1.6;
L2 = 4;

% Set to 'yes' if you would like to save data
saveData = 'yes';

% Define bounds for parameter space
minD1 = D1_hat/20;
maxD1 = D1_hat*5;
minD2 = D2_hat/20;
maxD2 = D2_hat*5;

% Npts determines how fine the mesh is. Mesh is size Npts by Npts
Npts = 21; % Npts = 2001 was selected in the thesis

% Thresholds for indicator function
epsilon = [1.5,1.0,0.5];

% Colour map below. Currently set up for three indicator thresholds
map = [
    0,204/255,102/255; % Green
    1,0,0; % Red
    0,102/255,204/255 % Blue
];

```

```

%% Background Set-up

if strcmp(q,'none')
    x_data = p;
    nx = 1; % Number of probes
else
    x_data = [p,q];
    nx = 2;
end

% Constructing the mesh in both vector and matrix form
D1_pts = linspace(minD1,maxD1,Npts);
D2_pts = linspace(minD2,maxD2,Npts);
[D1_mesh,D2_mesh] = meshgrid(D1_pts,D2_pts);
D1_test = D1_mesh(:,1);
D2_test = D2_mesh(:,1);

%% Generate Data

% Find appropriate point to stop temporal sampling
thresh = 0.99; % Once this temperature is reached, sampling stops
fun = @(t) Model_Solve(L2,t,D1_hat,D2_hat,L1,L2) - thresh;
t_end = fzero(fun,[0,10^10*L2^2/D2_hat]); % Initial guess is scaled accordingly
M = 100; % Number of temporal samples
delta_t = t_end/M;
t_data = delta_t:delta_t:t_end;

T_hat = Model_Solve(x_data,t_data,D1_hat,D2_hat,L1,L2);

%% Evaluate Indicator Function over Parameter Space

% Set up to evaluate indicator function at probes
Nsamples = Npts^2;
Neps = length(epsilon); % Number of different thresholds considered
I_eps = zeros(Nsamples,Neps); % Contains a collection of I for different epsilon

% Plot_heights is used to generate the figure. It keeps track of whether

```

```

% the indicator function is satisfied for a given parameter pair. In the
% case that a parameter pairs results in I = 1 for more than one epsilon,
% the strictest such epsilon is used.
Plot_heights = NaN(Nsamples,1);
epsilon = sort(epsilon,'descend');

% Loop over all the different parameter pairs
for ii = 1:Nsamples
    T_test = Model_Solve(x_data,t_data,D1_test(ii),D2_test(ii),L1,L2);
    % Loop over the different epsilon
    for jj = 1:length(epsilon)
        I_eps(ii,jj) = IndicatorFunc(epsilon(jj),T_test,T_hat);
        if I_eps(ii,jj) == 1
            Plot_heights(ii) = epsilon(jj);
        end
    end
end

%% Create a Figure

% Unravel the Plot_heights into a mesh for plotting
Plot_mesh = zeros(Npts,Npts);
for i = 1:Npts
    Plot_mesh(1:Npts,i) = Plot_heights((i-1)*Npts+1:i*Npts);
end

% Plot
figure
hold on
surf(D1_mesh,D2_mesh,Plot_mesh,'EdgeColor','none')

% Plot details
view(2)
colormap(map)
grid off
xlabel('$D_1$ (mm$^2$/s)', 'Interpreter', 'Latex')
ylabel('$D_2$ (mm$^2$/s)', 'Interpreter', 'Latex')
plot3(D1_hat,D2_hat,epsilon(Neps)+1,'ko','MarkerFaceColor',[0,0,0])

```

```

set(gca,'FontSize',16)
set(gca,'TickLabelInterpreter','Latex')
axis([minD1,maxD1,minD2,maxD2])
box on
set(gca,'Layer','top')

% Save data
if strcmp(saveData,'yes')
    Results = Plot_mesh;
    if nx == 1
        save(['ResultsForSingleProbeAt',num2str(10*p)],'Results')
    else
        save(['ResultsForTwoProbesAt',num2str(10*p),'and',num2str(10*q)],'Results')
    end
end

function I = IndicatorFunc(epsilon,T_test,T_hat)
% Author: Sean McInerney; Last Update: 28/02/2018
% Evaluates the Indicator Function.
%
% Refer to Equations (2.20) and (2.22)
%
% FUNCTION INPUTS:
% epsilon - Threshold for indicator function
% T_hat - The temperature data, evaluated using target parameters
% T_test - The temperature, evaluated using test parameters
% FUNCTION OUTPUT:
% I - The evaluated indicator function: either 1 or 0

d = sum(abs(T_hat-T_test),2); % Refer to Equation (2.19)

[nx,~] = size(T_hat); % Number of probes
if nnz(d <= epsilon) == nx % If all discrepancies are below epsilon
    I = 1;
else
    I = 0;
end

```

## Solution Verification.m

This script can be used to generate Figure 3.2. It requires the functions Model\_Solve.m, Laplace\_Temperature.m and cf.m. The script plots both the numerical solution and the semi-analytical solution to the mathematical model outlined in Equations (3.21)-(3.26). The semi-analytical solution is presented in Equations (3.39)-(3.40) and the numerical solution is presented in Equations (3.56)-(3.59).

```

%% Solution Verification
% Author: Sean McInerney; Last Update: 08/08/2018
%
% Used to generate Figure 3.2

%% Set-up

clear
clc
close all

% Parameters
D1 = 0.09;
D2 = 0.009;
L1 = 1.6;
L2 = 4;

% Spatial discretisation
N = 201; % Select N such that K is an integer
K = (N-1)*(L1/L2)+1;

% Find appropriate point to stop temporal sampling
thresh = 0.99; % Once this is reached, sampling stops
fun = @(t) Model_Solve(L2,t,D1,D2,L1,L2) - thresh;
t_c = fzero(fun,[0,10^10*L2^2/D2]); % Initial guess scaled
% Designate plot times
t_plot = [0.01,0.05,0.1,0.2,0.5,1]*t_c; % Plot times
nt = length(t_plot); % Number of plots

```

```

% Set up background colours
colour = [0.8275,0.5529,0.7176; 0.8745,0.8039,0.8784];

% Plot details
figure
hold on
rectangle('Position',[0,0,L1,1], 'FaceColor', colour(1,:),...
'EdgeColor','none')
rectangle('Position',[L1,0,L2-L1,1], 'FaceColor', colour(2,:),...
'EdgeColor','none')
xlabel('$x$ (mm)', 'Interpreter', 'Latex')
ylabel('Temperature', 'Interpreter', 'Latex')
set(gca,'FontSize',16)
set(gca,'TickLabelInterpreter','Latex')
axis([0,L2,0,1])
annotation('arrow',[0.2,0.7],[0.25,0.9], 'LineWidth',1.5)
box on

% Determine which nodes are plotted for numerical solution
nx = 11; % Number of bullet points in numerical visualisation
index = round(linspace(1,N,nx),0); % Assists in numerical visualisation

%% Semi-analytical Approach

x = linspace(0,L2,N); % Spatial points where solution is evaluated

soln = Model_Solve(x,t_plot,D1,D2,L1,L2); % Semi-analytical solution
for i = 1:nt
    plot(x,soln,'k','LineWidth',1.5);
end

%% Numerical Approach

% Discretisation
Delta_x = x(2) - x(1);
Delta_t = 10^(-6)*t_c;
t_current = Delta_t; % Keeps track of the time
% To ensure that the numerical solution is evaluated at the times

```

```

% designated in t_plot, Delta_t_current is introduced. It takes on the time
% until the next plot time, if t_current+Delta_t were to exceed the next
% plot time
Delta_t_current = Delta_t;
plot_count = 0; % How many of the plots have been plotted

% Initial time (Refer to Equation (3.47)-(3.48))
T = zeros(N,1); % T is the numerical approximation to the temperature
T(1) = 1; % Dirichlet BC (Refer to Equation (3.49))

% Construct A (Refer to Equations (3.57)-(3.59))
A_L = [D1*ones(1,K-1),D2*ones(1,N-K-1),2*D2];
A_D = [0,-2*D1*ones(1,K-2),-(D1+D2),-2*D2*ones(1,N-K)];
A_U = [0,D1*ones(1,K-2),D2*ones(1,N-K)];
A = sparse(diag(A_L,-1)+diag(A_D)+diag(A_U,1));

while plot_count < nt

    % Iterate through time (Refer to Equation (3.56))
    T = T + (Delta_t_current/Delta_x^2)*A*T;

    % Check if deltat needs to be changed to obtain plot time
    Delta_t_current = t_plot(plot_count+1) - t_current;
    if Delta_t_current > Delta_t
        Delta_t_current = Delta_t;
    end

    % Plot if necessary
    if t_current == t_plot(plot_count+1)
        plot_count = plot_count+1;
        plot(x(index),T(index),'k.', 'MarkerSize', 18)
    end

    % Increment time
    t_current = t_current + Delta_t_current;
end

```

**SolutionVisualisation.m**

This script can be used to generate Figure 2.2. It requires the functions Model\_Solve.m, Laplace\_Temperature.m and cf.m. All subfigures of Figure 2.2 are generated with one run of the script.

```
%% Solution Visualisation
% Author: Sean McInerney; Last Update: 14/06/2018
%
% Used to generate Figure 2.2

%% Set-up

clear
clc
close all

% Target parameters
D1_hat = 0.09;
D2_hat = 0.009;

% Spatial structure
L1 = 1.6;
L2 = 4;
N = 101;
x = linspace(0,L2,N);

% Probe location
p = L2;

% Set up background colours for Figure 2.2(a) and (c)
colour = [0.8275,0.5529,0.7176; 0.8745,0.8039,0.8784];

% Plot times
t_plot_a = [10,20,50,100,200,500,1000]; % For Figure 2.2(a)
t_plot_c = [10,200,500]; % For Figure 2.2(c)
```

```
% Parameters used for comparison in Figure 2.2(c)-(d)
D1 = [D1_hat,0.45];
D2 = [D2_hat,0.0077];

% Line colours in Figure 2.2(c)-(d)
% This would need to be adapted if more than two parameter pairs are compared
linecolours = [0,0,0; 0.15,0.65,0.15];

% Find appropriate point to stop temporal sampling
threshold = 0.99; % Once this temperature is reached at probe, sampling stops
fun = @(t) Model_Solve(p,t,D1_hat,D2_hat,L1,L2) - threshold;
t_c = fzero(fun,[0,10^10*L2^2/D2_hat]); % Initial guess is scaled

% Data points
M = 100; % Number of temporal samples
delta_t = t_c/M;
t_data = delta_t:delta_t:t_c;

% Generate synthetic temperature data
T_hat = Model_Solve(p,t_data,D1_hat,D2_hat,L1,L2);

%% Figure 2.2(a)

% Plot details
figure
hold on
rectangle('Position',[0,0,L1,1], 'FaceColor', colour(1,:), ...
'EdgeColor', 'none')
rectangle('Position',[L1,0,L2-L1,1], 'FaceColor', colour(2,:), ...
'EdgeColor', 'none')
xlabel('$x$ (mm)', 'Interpreter', 'Latex')
ylabel('Temperature', 'Interpreter', 'Latex')
axis([0,L2,0,1])
set(gca, 'FontSize', 16)
box on
set(gca, 'TickLabelInterpreter', 'Latex')
annotation('arrow',[0.2,0.7],[0.25,0.9], 'LineWidth', 1.5)
```

```
% Plot model solution
T = Model_Solve(x,t_plot_a,D1_hat,D2_hat,L1,L2);
plot(x,T,'k','LineWidth',1.5);

%% Figure 2.2(b)

% Plot details
figure
hold on
xlabel('$t$ (sec)', 'Interpreter', 'Latex')
ylabel('Temperature', 'Interpreter', 'Latex')
set(gca, 'FontSize', 16)
box on
set(gca, 'TickLabelInterpreter', 'Latex')
axis([0,1.2*t_c,0,1])
plot([t_c,t_c],[0,1], 'k--')

% Plot data
plot(t_data,T_hat, 'k.')

%% Figure 2.2(c)

% Plot details
figure
hold on
rectangle('Position', [0,0,L1,1], 'FaceColor', colour(1,:), 'EdgeColor', 'none')
rectangle('Position', [L1,0,L2-L1,1], 'FaceColor', colour(2,:), 'EdgeColor', 'none')
axis([0,4,0,1])
xlabel('$x$ (mm)', 'Interpreter', 'Latex')
ylabel('Temperature', 'Interpreter', 'Latex')
set(gca, 'FontSize', 16)
box on
set(gca, 'TickLabelInterpreter', 'Latex')
annotation('arrow', [0.2,0.7], [0.25,0.9], 'LineWidth', 1.5)

% Loop over the different parameter pairs
for ii = 1:length(D1)
    T_ii = Model_Solve(x,t_plot_c,D1(ii),D2(ii),L1,L2);
```

```

% Loop over plot times
for jj = 1:length(t_plot_c)
    % Plot solution using different parameter pairs
    plot(x,T_ii(:,jj),'Color',linecolours(ii,:),'LineWidth',1.5);
end

%% Figure 2.2(d)

% Plot details
figure
hold on
xlabel('$t$ (sec)', 'Interpreter', 'Latex')
ylabel('Temperature', 'Interpreter', 'Latex')
set(gca, 'FontSize', 16)
box on
set(gca, 'TickLabelInterpreter', 'Latex')
plot([t_c,t_c],[0,1], 'k--')
axis([0,1.2*t_c,0,1])

% Loop over different parameter pairs
for ii = 1:length(D1)
    % Plot solution at probe location using different parameter pairs
    T_ii = Model_Solve(p,t_data,D1(ii),D2(ii),L1,L2);
    plot(t_data,T_ii,'Color',linecolours(ii,:),'LineWidth',1.5)
end

```

## OptimalProbeLocation.m

This script can be used to generate Figure 2.5 and Figure 2.7. It requires the functions TestParameterSpace.m, Model\_Solve.m, Laplace\_Temperature.m and cf.m. The script determines  $\mathcal{A}_1$  for different choices of  $p$  and  $\mathcal{A}_2$  for different choices of  $q$ . This is very computationally expensive if a fine mesh of the parameter space is used to calculate  $\mathcal{A}_1$  and  $\mathcal{A}_2$ . In Figure 2.5 and Figure 2.7, over 4 million parameter pairs were tested for each choice of experimental design.

```
%% Optimal Probe Location
% Author: Sean McInerney; Last Update: 21/06/2018
%
% Used to generate Figures 2.5 and 2.7
%
% Uses TestParameterSpace.m to generate data
% Ensure that parameters in TestParameterSpace.m are appropriate and
% saveData = 'yes' is selected
%
% Is computational costly for high values of Npts

%% Set-up

clear
clc
close all

% Spatial Structure
L1 = 1.6;
L2 = 4;

% Different probe locations
PROBES = cell(40,1);
for ii = 1:20
    PROBES{ii} = 0.2*ii; % Single probe set-ups
    PROBES{ii+20} = [4,0.2*ii]; % Two probe set-ups
end

% Thresholds for indicator function.
epsilon = [1.5,1.0,0.5];

% Colour scheme of lines. Currently set up for three thresholds
map = [
    0,102/255,204/255 % Blue
    1,0,0; % Red
    0,204/255,102/255; % Green
];
```

```

% Set-up background colours
colour = [0.8275,0.5529,0.7176; 0.8745,0.8039,0.8784];

%% Generate Data using TestParameterSpace.m

% Loop over different probe set-ups
for ii = 1:length(PROBES)
    p = PROBES{ii}(1);
    if length(PROBES{ii})==2 % If there is a second probe
        q = PROBES{ii}(2);
    else
        q = 'none';
    end
    TestParameterSpace(p,q) % Generate data
end

close all

%% Work with Data

nP = length(PROBES); % Number of different probe set-ups
Neps = length(epsilon); % Number of different thresholds considered
% mathcalA will contain the proportion of area where I = 1 for each
% probe set-up and each choice of epsilon.
mathcalA = zeros(nP,Neps);
nSP = 0; % Number of single probe set-ups investigated
n2P = 0; % Number of two probe set-ups investigated
% To determine nSp and n2P:
for ii = 1:nP
    x_data = PROBES{ii}; % Probe locations in this set-up
    nx = length(x_data);
    if nx == 1
        nSP = nSP+1;
    elseif nx == 2
        n2P = n2P+1;
    end
end

```

```

singleProbeIndex = zeros(nSP,1); % Keeps track of 1 probe set-ups
twoProbeIndex = zeros(n2P,1); % Keeps track of 2 probe set-ups

singleProbes = zeros(nSP,1); % Locations of single probes
twoProbes = zeros(n2P,1); % 2nd probe in 2 probe set-ups

for ii = 1:nP % Loop over probe set-ups
    x_data = PROBES{ii};
    nx = length(x_data);
    p = x_data(1);
    if nx == 1 % If it is a single probe set up
        load(['ResultsForSingleProbeAt',num2str(10*p)])
        for jj = 1:Neps % Loop over different choices of epsilon
            % Find the parameter pairs where I_1(D1,D2|p,eps) \leq epsilon
            mathcalA(ii,jj) = length(find(Results<=epsilon(jj)));
        end
        index = find(singleProbeIndex==0,1); % Find next index to adjust
        singleProbeIndex(index) = ii;
        singleProbes(index) = p; % Store the probe location
    elseif nx == 2 % If it is a two probe set-up
        q = x_data(2);
        load(['ResultsForTwoProbesAt',num2str(10*p),',and,',num2str(10*q)])
        for jj = 1:Neps % Loop over different choices of epsilon
            % Find the parameter pairs where I_1(D1,D2|p,eps) \leq epsilon
            mathcalA(ii,jj) = length(find(Results<=epsilon(jj)));
        end
        index = find(twoProbeIndex==0,1); % Find next index to adjust
        twoProbeIndex(index) = ii;
        twoProbes(index) = q; % Store the second probe location
    end
    mathcalA(ii,:) = mathcalA(ii,:)/numel(Results); % Scale area
end

%% Produce plot

% If any single probe set-ups have been considered
if nSP > 0

```

```
% Plot details
figure5 = figure;
axes5 = axes('parent',figure5);
hold on

maxSingle = max(mathcalA(singleProbeIndex));
rectangle(axes5,'Position',[0,0,L1,1.2*maxSingle],...
'FaceColor',colour(1,:),'EdgeColor','none')
rectangle(axes5,'Position',[L1,0,L2-L1,1.2*maxSingle],...
'FaceColor',colour(2,:),'EdgeColor','none')
axis(axes5,[0,L2,0,1.2*maxSingle])
box on
set(axes5,'FontSize',12)
xlabel(axes5,'$p\$ (mm)', 'Interpreter','Latex')
ylabel(axes5,'$\mathcal{A}_1$', 'Interpreter','Latex')
set(axes5,'TickLabelInterpreter','Latex')

% Pre-plot sorting of indices
[singleProbes,index] = sort(singleProbes);
singleProbeIndex = singleProbeIndex(index);

% Plot
for jj = 1:Neps
    plot(axes5,singleProbes,mathcalA(singleProbeIndex,jj),...
    '.', 'Color',map(jj,:),'MarkerSize',18)
    plot(axes5,singleProbes,mathcalA(singleProbeIndex,jj),...
    '--', 'Color',map(jj,:),'LineWidth',1.5)
end
end

% If any two probe set-ups have been considered
if n2P > 0

    % Plot details
    figure7 = figure;
    axes7 = axes('parent',figure7);
    hold on
```

```
maxTwo = max(mathcalA(twoProbeIndex));
rectangle(axes7,'Position',[0,0,L1,1.2*maxTwo],...
'FaceColor',colour(1,:),'EdgeColor','none')
rectangle(axes7,'Position',[L1,0,L2-L1,1.2*maxTwo],...
'FaceColor',colour(2,:),'EdgeColor','none')
axis(axes7,[0,L2,0,1.2*maxTwo])
box on
set(axes7,'FontSize',12)
xlabel(axes7,'$q\$ (mm)', 'Interpreter', 'Latex')
ylabel(axes7,'$\mathcal{A}_2$', 'Interpreter', 'Latex')
set(axes7,'TickLabelInterpreter', 'Latex')

% Pre-plot sorting of indices
[twoProbes,index] = sort(twoProbes);
twoProbeIndex = twoProbeIndex(index);

% Plot
for jj = 1:Neps
    plot(axes7,twoProbes,mathcalA(twoProbeIndex,jj),...
        '.', 'Color',map(jj,:), 'MarkerSize',18)
    plot(axes7,twoProbes,mathcalA(twoProbeIndex,jj),...
        '--', 'Color',map(jj,:), 'LineWidth',1.5)
end
end
```